F-Actin Bending Facilitates Net Actomyosin Contraction By Inhibiting Expansion With Plus-End-Located Myosin Motors

Alexander K. Y. Tam^{*1}**, Alex Mogilner**^{2}**, and Dietmar B. Oelz**^{1}

^{1}School of Mathematics and Physics, The University of Queensland, St Lucia, Queensland 4072, Australia.

^{2}Courant Institute of Mathematical Sciences, New York University, New York, NY, USA

August 20, 2021

Abstract

We investigate whether a microscopic system of two semi-flexible actin filaments with an attached myosin motor can facilitate contraction. Based on energy minimisation, we derive and analyse a partial differential equation model for a two-filament-motor structure embedded within a dense, two-dimensional network. Our method enables calculation of the plane stress tensor, providing a measure for contractility. After deriving the model, we use a combination of asymptotic analysis and numerical solutions to show how F-actin bending facilitates net contraction as a myosin motor traverses two symmetric filaments. Myosin motors close to the minus-ends facilitate contraction, whereas motors close to the plus-ends facilitate expansion. The leading-order solution for rigid filaments exhibits polarity-reversal symmetry, such that the contractile and expansive components balance to zero. Surprisingly, after introducing bending the first-order correction to stress indicates expansion. However, numerical solutions show that filament bending induces a geometric asymmetry that brings the filaments closer to parallel as a myosin motor approaches their plus-ends. This decreases the effective spring force opposing motion of the motor, enabling it to move faster close to filament plus-ends. This reduces the contribution of expansive stress, giving rise to net contraction. Further numerical solutions confirm that this applies beyond the small bending regime considered in the asymptotic analysis. Our findings confirm that filament bending gives rise to microscopic-scale actomyosin contraction, and provides a possible explanation for network-scale contraction.

Keywords: actomyosin, curve-straightening flow, energy functional, gradient flow, stress tensor, asymptotic analysis

1   Introduction

The mechanics of actin filament and myosin motor proteins in the cell cortex underpins movement (Yamada and Sixt 2019) and division (Pollard 2010) of biological cells. Early

---

*Corresponding author: alex.tam@uq.edu.au

breakthroughs in understanding actomyosin dynamics occurred in the context of muscle cells (Gautel 2011). There, actin and myosin form sarcomere structures, in which filaments are aligned in parallel with minus-ends in the centre and plus-ends pointing outwards. Relative motion of myosin motors towards filament plus-ends subsequently generates contraction by pulling filaments inwards. This mechanism is known as sliding filament theory (Huxley 2004). However, actomyosin networks in the cell cortex are disordered, with filaments distributed at random. Experiments (Murrell, Oakes, et al. 2015; Pollard and O'Shaughnessy 2019) and simulations (Tam, Mogilner, and Oelz 2021; Ennomani et al. 2016) have shown that disordered actomyosin networks also contract (Chalut and Paluch 2016). Sliding filament theory predicts that random networks would produce expansion or contraction with equal probability, and thus cannot explain this contraction. Consequently, the origin of contraction in disordered networks remains an active field of research. A pertinent question is whether asymmetry on the microscopic scale (Lenz 2014; Komianos and Papoian 2018) can explain network-scale contraction, or whether long-range effects amplify contractile stress (Ronceray, Broedersz, and Lenz 2016). A microscopic asymmetry would require additional mechanics to those predicted by sliding filament theory.

Filament bending flexibility is commonly-hypothesised as a source of asymmetry that might explain contraction of disordered actomyosin networks (Murrell and Gardel 2012; De La Cruz and Gardel 2015; du Roure et al. 2019; Head, Levine, and MacKintosh 2003; Tam, Mogilner, and Oelz 2021). Actin filaments are semi-flexible (Stachowiak et al. 2014; Belmonte, Leptin, and Nédélec 2017), such that they undergo small but significant bending (Broedersz and Mackintosh 2014; Murrell and Gardel 2012). This is not relevant in sarcomeres with parallel arrays of filaments, but is for two and three-dimensional networks with random filament orientations. Many previous experimental and theoretical studies invoke a filament buckling mechanism, whereby filaments can sustain longitudinal tension, but buckle under longitudinal compression (Bidone et al. 2017; Belmonte, Leptin, and Nédélec 2017; Cheffings, Burroughs, and Balasubramanian 2016; du Roure et al. 2019; Freedman, Banerjee, et al. 2017; Freedman, Hocky, et al. 2018; Lenz 2020; Murrell and Gardel 2012; Ronceray, Broedersz, and Lenz 2016; Soares e Silva et al. 2011; Yu et al. 2018). This has been shown to generate network-scale bias to contraction over expansion (Belmonte, Leptin, and Nédélec 2017). Other studies have considered a related filament bending mechanism (Lenz 2014; Tam, Mogilner, and Oelz 2021; Head, Levine, and MacKintosh 2003; Popov, Komianos, and Papoian 2016; Kim 2015; Letort et al. 2015) as a source of force asymmetry. This involves applying forces that pluck filaments transversely, as opposed to the longitudinal forces involved with buckling. Lenz (2014) showed that filament bending produces forces that exceed those involved with longitudinal buckling, and Tam, Mogilner, and Oelz (2021) showed that this mechanism facilitates network-scale contraction.

An interesting question is whether the force asymmetry provided by bending or buckling

applies at the microscopic scale. De La Cruz and Gardel (2015) state that compression, stretching, and bending forces are relevant on the small scale. In contrast, Ronceray, Broedersz, and Lenz (2016) state that buckling facilitates network-scale contraction by enabling transmission of contractile force, and inhibiting expansive. This phenomenon is highly nonlinear, and does not require microscopic asymmetry. One approach to understand microscopic filament dynamics is to model a single filament as a worm-like chain (Broedersz and Mackintosh 2014; Lenz et al. 2012). Broedersz and Mackintosh (2014) used this approach to identify an asymmetry under extension and compression. Other authors have considered structures consisting of two-filaments and an attached motor (Lenz 2014; Belmonte, Leptin, and Nédélec 2017; Hiraiwa and Salbreux 2016; Komianos and Papoian 2018). Hiraiwa and Salbreux (2016) and Komianos and Papoian (2018) considered the effect of motors and cross-linkers on forces generated by rigid filament pairs. However, Lenz (2014) reported that disordered networks of rigid filaments with polarity-reversal symmetry (*i.e.* any configuration of filaments is equally likely as the same configuration with minus and plus-ends reversed) generate zero net contraction. Belmonte, Leptin, and Nédélec (2017) developed a statistical method to predict network-scale contraction by summing the contributions from two-filament structures, assuming filaments buckle under compression. An important advance was provided by Lenz (2014), who compared symmetry-breaking mechanisms for two filaments, and found filament bending gives rise to contraction on the microscopic scale. They subsequently showed bending to be the dominant mechanism of contraction for experimentally-feasible parameters. Our objective is to investigate the microscopic origin of bending-induced contraction in detail.

Semi-flexible filament evolution is an example of a curve-straightening flow. Mathematically, this refers to deformation of curves in $\mathbb{R}^2$ by decreasing their total squared curvature. Curve-straightening is relevant to actomyosin, because filaments evolve to minimise their bending energy, which is proportional to total curvature. Curve-straightening problems have been investigated extensively since the 1980s, mostly in the context of single curves (Langer and Singer 1984; Langer and Singer 1987; Linnér 1989; Linnér 2003). Wen (1993) and Wen (1995) then used the indicatrix representation and L^2-gradient flow of the squared curvature functional to derive a fourth-order, semilinear parabolic partial differential equation (PDE). Oelz (2011) extended these methods to open curves. However, current theoretical analysis of curve-straightening flows is largely limited to single curves. In this work, we extend these methods to pairs of curves interacting with a molecular motor, and derive and analyse the associated partial differential equations.

The objectives of this paper are two-fold. First, we derive a PDE model for two semi-flexible filaments with a myosin motor attached at their intersection. Through this derivation, we describe how to obtain an explicit formula for the network stress tensor. We then use this model to investigate in detail how this two-filament structure facilitates microscopic-scale contraction. Since these dynamics are more complex than the single-

curve straightening problem, we use a combination of asymptotic analysis and numerical solutions to achieve this. We apply the model to pairs of symmetric filaments with a motor initially attached to the minus-ends, and solve until the motor reaches the plus-ends and detaches. From this analysis, we propose a mechanism based neither on filament buckling, nor intrinsic force asymmetry where bending generates contraction. Instead, we find that filament semi-flexibility creates a geometric asymmetry that inhibits expansion. Two rigid filaments exhibit polarity-reversal symmetry, such that the contraction associated with a minus-end-located motor balances with expansion associated with a plus-end-located motor. Introducing filament bending breaks this symmetry, and brings the filaments closer to parallel as the motor approaches the plus-ends. This decreases the resistance to motion generated by the spring force through the motor, enabling it to move faster close to the plus-ends. This asymmetry inhibits expansive stress, and gives rise to net contraction on the microscopic scale.

2 Mathematical Model

We develop a mathematical model for a myosin motor attached to two overlapping actin filaments, as illustrated in Figure 2.1a. We represent filaments as open curves in $\mathbb{R}^2$, and denote their positions by $z_i(s(t), t) = (x_i(s(t), t), y_i(s(t), t))$, for $i = 1, 2$. Here, t is time and $s \in [0, L_i]$ is the arc length parameter, where L_i is the length of the i-th filament. Since actin filaments are polarised, we adopt the convention that $s = 0$ corresponds to the filament minus-end, and $s = L_i$ corresponds to the plus-end. We represent the myosin motor as a point object existing at the intersection between the two filaments. We track its position by introducing the variables $m_i(t) \in [0, L_i]$, such that $s = m_i$ is the position of the motor head attached to the i-th filament. We assume that no other proteins, for example cross-linkers, are present. The two-filament-motor system is located within a parallelogram-shaped domain, the adjacent sides of which are given by the vectors $\boldsymbol{L}_x = (L_{xx}, L_{xy})^T$, and $\boldsymbol{L}_y = (L_{yx}, L_{yy})$. The vectors $\boldsymbol{F}_x = (F_{xx}, F_{xy})$ and $\boldsymbol{F}_y = (F_{yx}, F_{yy})$, shown in Figure 2.1a, are the normal and shear force components acting on the domain boundaries. These can be obtained as part of the solution, and we will describe the method to compute these later.

We express the mathematical model for the filament and motor mechanics as a system of force-balance equations. In abstract terms, we write

$$F_{a,\text{drag}} - \delta E_{a,\text{bend}} - \delta E_{a,\text{stretch}} - \delta E_{m,\text{stretch}} + F_{m,a} = \mathbf{o}. \tag{2.1}$$

The first three terms in (2.1) describe the drag, bending, and longitudinal stretching forces respectively on actin filaments. The fourth term represents longitudinal stretching along the myosin motor, and the final term describes forces between filaments and motors.
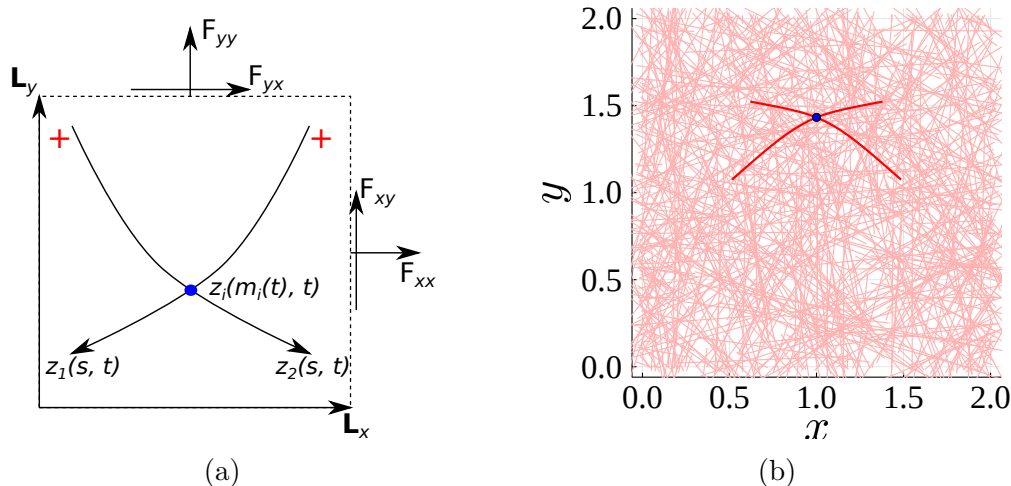
4

Figure 2.1: (a) Schematic representation of a two-filament-motor system. The filaments are the curves z_1 and z_2, and arrow heads represent filament minus (pointed) ends. Myosin motor proteins are represented by blue dots, and initially appear at the intersection between the two filaments. (b) A two-filament-motor structure immersed in a dense background network.

We represent bending and stretching forces as the variation of potential energy, where terms involving δ denote variations. We conceptualise drag as the combined effects of friction between the filaments and the cytoplasm, and protein friction (Tam, Mogilner, and Oelz 2021; McFadden et al. 2017; Bormuth et al. 2009; Tawada and Sekimoto 1991) acting at intersections between the two filaments and filaments in a background network. Figure 2.1b illustrates this scenario. In the limit of infinite background network density, protein friction acts uniformly along the two filaments in consideration, and represents the dominant contribution to overall drag.

2.1 Energy Minimisation and Calculation of Stress

To derive and simulate the model, we formulate the force-balance equations (2.1) as an energy minimisation problem. This involves constructing a time-discrete functional that sums the contribution of each force term,

$$E\left[z_1, z_2, m_1, m_2\right] := E_{a,\text{drag}} + E_{a,\text{bend}} + E_{a,\text{stretch}} + E_{m,\text{stretch}} + E_{m,a}. \qquad (2.2)$$

In (2.2), $E_{a,\text{bend}}$, $E_{a,\text{stretch}}$, and $E_{m,\text{stretch}}$ are the potential energies associated with filament bending, filament stretching, and motor stretching respectively. The terms $E_{a,\text{drag}}$ and $E_{m,a}$ are pseudo-energy terms with variations that correspond to finite-difference approximations of $F_{a,\text{drag}}$ and $F_{m,a}$, which cannot be interpreted as variations of potential energy. At each time step of the simulation, the filament and motor positions are the minimiser of the functional (2.2). We outline each term in (2.2) below.

5

The first term, $E_{a,\mathrm{drag}}$, describes drag friction that opposes filament motion. Drag acts uniformly along the filaments, and could arise from viscous drag between filaments and the cytoplasm, or from protein friction between the filaments and a dense background network. The pseudo-energy term to represent this is

$$E_{a,\mathrm{drag}} = \lambda_a \sum_{i=1}^{2} \int_0^{L_i} \frac{|z_i - \boldsymbol{F} z_i^n|^2}{2 \Delta t} \, \mathrm{d}s, \tag{2.3}$$

where λ_a is the filament drag coefficient, Δt is the time step size, and the superscript n refers to the previous time step, *i.e.* $z_i^n = z_i(s, t - \Delta t)$. To account for possible stretching and rotation of the domain over time, we introduce the deformation gradient tensor,

$$\boldsymbol{F} = \begin{bmatrix} L_{xx}/L_{xx}^n & L_{yx}/L_{yy}^n \\ L_{xy}/L_{xx}^n & L_{yy}/L_{yy}^n \end{bmatrix}, \tag{2.4}$$

such that multiplying z_i^n by $\boldsymbol{F}$ ensures that z_i and z_i^n are both represented in the current spatial co-ordinates.

We model bending of semi-flexible actin filaments via the elastic potential energy

$$E_{a,\mathrm{bend}} = \sum_{i=1}^{2} \int_0^{L_i} \frac{\kappa_a}{2} |z_i''|^2 \, \mathrm{d}s, \tag{2.5}$$

where κ_a is the flexural rigidity, and primes denote differentiation with respect to arc-length, s. We assume that κ_a is constant, and the same for both filaments. We obtain a term for filament stretching by assuming that actin filaments are inextensible. To model this, we ensure that $|z_i'| = 1$ at every point along the filaments using the penalisation term

$$E_{a,\mathrm{stretch}} = \sum_{i=1}^{2} \int_0^{L_i} \frac{1}{\delta_a} \left(|z_i'| - 1 \right)^2 \, \mathrm{d}s, \tag{2.6}$$

where δ_a is an arbitrarily small parameter that enforces the inextensibility constraints.

The remaining two terms in (2.2) describe how motors contribute to the mechanics. We ensure that motors remain point objects by introducing another penalising potential,

$$E_{m,\mathrm{stretch}} = \frac{1}{\delta_m} \left| z_1(m_1, t) - z_2(m_2, t) \right|^2, \tag{2.7}$$

where δ_m is an arbitrarily small parameter that penalises deviation from the constraint $z_1(m_1, t) = z_2(m_2, t)$. The final term in (2.2) describes interactions between filaments and motors. We assume that motors obey a linear (affine) force-velocity relationship. Subject to zero force, motors move with speed V_m. As the force through the motor increases, velocity decreases linearly until the motor stops, which occurs at the force F_s, known as the stall force. The corresponding pseudo-energy term consists of a linear term, and a

6

quadratic drag-like term for the velocity reduction caused by the force through the motor,

$$E_{m,a} = \sum_{j=1}^{2} \left(-F_s \, m_j + \frac{F_s}{V_m} \frac{\left(m_j - m_j^n \right)^2}{2\Delta t} \right). \tag{2.8}$$

Minimising the functional (2.2) consisting of (2.3) and (2.5)–(2.8), then provides a time-implicit numerical method to solve for the filament and motor positions.

Another advantage of energy minimisation is that it enables direct calculation of forces on the domain boundary that must be applied to prevent elongation and shear. These forces sum the contributions of both filaments and the motor, and provide a measure of net contractility. We obtain these forces $\boldsymbol{F}_x$ and $\boldsymbol{F}_y$ by adding extra terms to the energy functional, and defining

$$E_{\text{total}} := E + \boldsymbol{F}_x \cdot \boldsymbol{L}_x + \boldsymbol{F}_y \cdot \boldsymbol{L}_y. \tag{2.9}$$

If we impose that $\boldsymbol{L}_x$ and $\boldsymbol{L}_y$ remain constant, the vectors $\boldsymbol{F}_x = -\partial_{\boldsymbol{L}_x} E$ and $\boldsymbol{F}_y = -\partial_{\boldsymbol{L}_y} E$ represent Lagrange multipliers that enforce the constant domain size and shape constraints. After computing these, we describe the two-dimensional state of stress in the domain using the plane stress tensor,

$$\boldsymbol{\sigma} = \begin{bmatrix} F_{xx}/L_{yy} & F_{xy}/L_{yy} \\ F_{yx}/L_{xx} & F_{yy}/L_{xx} \end{bmatrix}. \tag{2.10}$$

The bulk stress,

$$\sigma = \frac{1}{2}\text{tr}\left(\boldsymbol{\sigma} \right), \tag{2.11}$$

then provides a measure of the contraction or expansion generated by the two-filament-motor system. By convention, negative σ indicates contraction, and positive σ indicates expansion. The quantity σ is invariant to domain rotations, and equal to the average of the eigenvalues of $\boldsymbol{\sigma}$. The associated eigenvectors of $\boldsymbol{\sigma}$ are the principal stress directions, which indicate the directions of maximum contraction or expansion.

2.2 Governing Equations

Formulating the model as an energy minimisation problem enables us to derive PDEs that govern the filament and motor positions. The derivation is based on the following variational principle. It requires that, given known data $(z_1^n, z_2^n, m_1^n, m_2^n)$ at the discrete point in time n, the solution at the following point in time minimises the functional (2.2),

$$\left(z_1^{n+1}, z_2^{n+1}, m_1^{n+1}, m_2^{n+1} \right) = \text{argmin} \, E \left[z_1^n, z_2^n, m_1^n, m_2^n \right] (z_1, z_2, m_1, m_2). \tag{2.12}$$

We obtain the corresponding force-balance equations by setting to zero the functional derivatives of (2.2) with respect to filament and motor positions. Subsequently, we write

$$\delta E\left[z_1^n, z_2^n, m_1^n, m_2^n\right]\left(z_1^{n+1}, z_2^{n+1}, m_1^{n+1}, m_2^{n+1}\right) \cdot (\delta z_1, \delta z_2, \delta m_1, \delta m_2) = 0, \qquad (2.13)$$

where terms involving δ denote the variation of the respective quantity. This formulation enables us to write (2.1) in terms of z_i and m_i. We obtain the governing equations by evaluating (2.13) and matching coefficients of δz_1, δz_2, δm_1, and δm_2. On taking the formal continuum limit $\Delta t \to 0$, for which $\boldsymbol{F} \to \boldsymbol{I}$ and $(u - u^n)/\Delta t \to \dot{u}$, we obtain the system of PDEs

$$\begin{cases} \lambda_a \dot{z}_1 + \kappa_a z_1'''' - (\lambda_1 z_1')' + \mu \dfrac{z_1 - z_2}{\|z_1 - z_2\|} \delta(s - m_1) = 0, & (2.14a) \\[2ex] \lambda_a \dot{z}_2 + \kappa_a z_2'''' - (\lambda_2 z_2')' - \mu \dfrac{z_1 - z_2}{\|z_1 - z_2\|} \delta(s - m_2) = 0, & (2.14b) \\[2ex] \dot{m}_1 = V_m \left[1 - \dfrac{\mu}{F_s} \dfrac{z_1 - z_2}{\|z_1 - z_2\|} \cdot z_1'(m_1, t)\right], & (2.14c) \\[2ex] \dot{m}_2 = V_m \left[1 + \dfrac{\mu}{F_s} \dfrac{z_1 - z_2}{\|z_1 - z_2\|} \cdot z_2'(m_2, t)\right], & (2.14d) \end{cases}$$

where primes denote differentiation with respect to arc length, dots represent time derivatives, and $\delta(\cdot)$ is the Dirac delta function (not to be confused with variation). These equations (2.14) are a system of continuum force-balance equations for the filament and motor positions. They are formulated in a formal limit where δ_a and δ_m are small, and the force coefficients $1/\delta_a$ and $1/\delta_m$ in the variations of the penalising potentials (2.6) and (2.7) are replaced by the Lagrange multipliers λ_1, λ_2, and μ. Note that the sign of $z_1 - z_2$ in (2.14) will be absorbed by μ. As a consequence, solutions satisfy the constraints

$$\begin{cases} |z_i'| \equiv 1, & (2.15a) \\[1.5ex] z_1(m_1, t) = z_2(m_2, t). & (2.15b) \end{cases}$$

The equations are subject to the boundary conditions

$$\begin{cases} z_i''(0, t) = z_i''(L_i, t) = 0, & (2.16a) \\[1.5ex] (\kappa_a z_i''' - \lambda_i z_i')|_{s=0, L_i} = 0. & (2.16b) \end{cases}$$

A detailed derivation of (2.14) and (2.16) is provided in Appendix A.

To obtain an expression for the bulk stress, σ, we differentiate the energy functional (2.9)

with respect to $\boldsymbol{L}_x$ and $\boldsymbol{L}_y$. This yields

$$\boldsymbol{F}_x = \lambda_a \sum_{i=1}^{2} \int_0^{L_i} \frac{x_i^n}{L_{xx}^n} \frac{(z_i - \boldsymbol{F} z_i^n)}{\Delta t} \, \mathrm{d}s, \tag{2.17a}$$

$$\boldsymbol{F}_y = \lambda_a \sum_{i=1}^{2} \int_0^{L_i} \frac{y_i^n}{L_{yy}^n} \frac{(z_i - \boldsymbol{F} z_i^n)}{\Delta t} \, \mathrm{d}s. \tag{2.17b}$$

Then, applying the formal continuum limit $\Delta t \to 0$, $\boldsymbol{F} \to \boldsymbol{I}$, $(u - u^n)/\Delta t \to \dot{u}$, and $z_i^n \to z_i$, we obtain

$$\boldsymbol{F}_x = \lambda_a \sum_{i=1}^{2} \int_0^{L_i} \frac{x_i}{L_{xx}} \frac{\partial z_i}{\partial t} \, \mathrm{d}s, \tag{2.18a}$$

$$\boldsymbol{F}_y = \lambda_a \sum_{i=1}^{2} \int_0^{L_i} \frac{y_i}{L_{yy}} \frac{\partial z_i}{\partial t} \, \mathrm{d}s. \tag{2.18b}$$

Evaluating the bulk stress (2.11) then yields

$$\sigma = \lambda_a \sum_{i=1}^{2} \int_0^{L_i} \frac{x_i}{L_{xx}} \frac{\partial x_i}{\partial t} + \frac{y_i}{L_{yy}} \frac{\partial y_i}{\partial t} \, \mathrm{d}s = \lambda_a \sum_{i=1}^{2} \int_0^{L_i} z_i \cdot \frac{\partial z_i}{\partial t} \, \mathrm{d}s. \tag{2.19}$$

Furthermore, the expressions (2.18) confirm that

$$\begin{aligned}
\sigma_{xy} - \sigma_{yx} &= \lambda_a \sum_{i=1}^{2} \int_0^{L_i} \frac{x_i}{L_{xx} L_{yy}} \frac{\partial y_i}{\partial t} - \frac{y_i}{L_{xx} L_{yy}} \frac{\partial x_i}{\partial t} \, \mathrm{d}s \\
&= \frac{\lambda_a}{L_{xx} L_{yy}} \sum_{i=1}^{2} \int_0^{L_i} \begin{bmatrix} -y_i \\ x_i \end{bmatrix} \cdot \frac{\partial z_i}{\partial t} \, \mathrm{d}s \\
&= \frac{\lambda_a}{L_{xx} L_{yy}} \sum_{i=1}^{2} \int_0^{L_i} z_i^{\perp} \cdot \frac{\partial z_i}{\partial t} \, \mathrm{d}s = 0,
\end{aligned} \tag{2.20}$$

141 where $z_i^{\perp}$ denotes a vector orthogonal to z_i, and we obtain the result by substituting (2.14)
142 for $\dot{z}_i$. The stress tensor (2.10) is thus symmetric, as expected. Thus, the bulk stress σ is
143 equal to the average of the eigenvalues of $\boldsymbol{\sigma}$.

144 ## 2.3   Nondimensionalisation

We nondimensionalise the PDE model (2.14)–(2.16) by introducing the length and time scales

$$\hat{t} = \frac{F_s}{\lambda_a L_a^2} t, \quad \text{and} \quad (\hat{x}, \hat{y}) = \frac{1}{L_a} (x, y), \tag{2.21}$$

9

where hats represent dimensionless variables, and L_a is a characteristic filament length. The dimensionless model is then (dropping hats for convenience)

$$
\begin{cases}
\dot{z}_1 + \kappa^* z_1'''' - (\lambda_1^* z_1')' + \mu^* \dfrac{z_1 - z_2}{\|z_1 - z_2\|} \delta^*(s - m_1) = 0, & \text{(2.22a)} \\[2ex]
\dot{z}_2 + \kappa^* z_2'''' - (\lambda_2^* z_2')' - \mu^* \dfrac{z_1 - z_2}{\|z_1 - z_2\|} \delta^*(s - m_2) = 0, & \text{(2.22b)} \\[2ex]
\dfrac{1}{V_m^*} \dot{m}_1 = 1 - \mu^* \dfrac{z_1 - z_2}{\|z_1 - z_2\|} \cdot z_1'(m_1, t), & \text{(2.22c)} \\[2ex]
\dfrac{1}{V_m^*} \dot{m}_2 = 1 + \mu^* \dfrac{z_1 - z_2}{\|z_1 - z_2\|} \cdot z_2'(m_2, t), & \text{(2.22d)}
\end{cases}
$$

subject to the boundary conditions

$$
\begin{cases}
z_i''(0, t) = z_i''(L_i^*, t) = 0, & \text{(2.23a)} \\[1.5ex]
\left. (\kappa^* z_i''' - \lambda_i^* z_i') \right|_{s=0, L_i^*} = 0, & \text{(2.23b)}
\end{cases}
$$

and the constraints

$$
\begin{cases}
|z_i'| \equiv 1, & \text{(2.24a)} \\[1.5ex]
z_1(m_1, t) = z_2(m_2, t), & \text{(2.24b)}
\end{cases}
$$

where $\delta^*(\hat{x}) = L_a \delta(L_a \hat{x})$ is a scaled Dirac delta function. The dimensionless parameters and forces are

$$
\kappa^* = \frac{\kappa}{F_s L_a^2}, \quad \lambda_i^* = \frac{\lambda_i}{F_s}, \quad \mu_i^* = \frac{\mu_i}{F_s}, \quad V_m^* = \frac{V_m \lambda_a L_a}{F_s}, \quad \text{and} \quad L_i^* = \frac{L_i}{L_a}. \tag{2.25}
$$

In subsequent sections, we consider asymptotic analysis and numerical solutions to the dimensionless system (2.22) and (2.23).

2.4 Symmetric Filament–Motor Assemblies

Before proceeding with the analysis, we consider a simplification to (2.22) and (2.23). First, we assume that the two filaments are symmetric about the vertical, that is

$$
z_1 = z, \quad z_2 = \begin{bmatrix} -1 & 0 \\ 0 & 1 \end{bmatrix} z, \tag{2.26}
$$

and have identical length $L_1 = L_2 = L_a$. This symmetry also implies that the relative position of the motor is the same for both filaments, $m_1 = m_2 = m$, and that $\lambda_1^* = \lambda_2^* = \lambda^*$. To simplify the motor dynamics (2.22c) and (2.22d), we impose $V_m \to \infty$. Finally, we assume that filaments have large flexural rigidity $\kappa^* = 1/\varepsilon$, where $\varepsilon \ll 1$, and thus undergo small bending. On applying these simplifications, the dimensionless model (2.22) becomes

(dropping asterisks on dimensionless parameters)

$$\begin{cases} \dfrac{\partial z}{\partial t} + \dfrac{1}{\varepsilon} z'''' - (\lambda z')' + \mu \begin{pmatrix} 1 \\ 0 \end{pmatrix} \delta(s - m), & \text{(2.27a)} \\[12pt] 0 = 1 - \mu \begin{pmatrix} 1 \\ 0 \end{pmatrix} \cdot z'(m(t), t), & \text{(2.27b)} \end{cases}$$

subject to the boundary and initial conditions

$$\begin{cases} z''(0,t) = z''(1,t) = 0, & \text{(2.28a)} \\[8pt] \left(\dfrac{1}{\varepsilon} z''' - \lambda z' \right)\Big|_{s=0,1} = 0, & \text{(2.28b)} \\[8pt] z(s, t=0) = z_I(s), & \text{(2.28c)} \end{cases}$$

and the constraints

$$\begin{cases} |z'| = 1, & \text{(2.29a)} \\[8pt] z(m(t), t) = \begin{pmatrix} 0 \\ y(t) \end{pmatrix}. & \text{(2.29b)} \end{cases}$$

The dimensionless form of the bulk stress (2.19) in the simplified model (2.27) and (2.28) is then

$$\sigma = 2 \int_0^1 \frac{\partial z}{\partial t} \cdot z \, \mathrm{d}s = -2 \int_0^1 \frac{1}{\varepsilon} (z'')^2 + \lambda \, \mathrm{d}s. \tag{2.30}$$

To obtain a measure of net stress, we integrate σ over the time between motor attachment and detachment. This yields

$$\int_0^T \sigma \, \mathrm{d}t = J(T) - J(0), \tag{2.31}$$

where

$$J(t) = \int_0^1 |z(s,t)|^2 \, \mathrm{d}s. \tag{2.32}$$

The quantity $J(T) - J(0)$ describes the net, time-aggregated stress that the two filaments produce as they evolve. With this in mind, we use a combination of asymptotic analysis and numerical solutions to investigate the effect of filament bending on contraction.

11

3 Asymptotic Analysis

We construct an asymptotic approximation to the solution of the model for the simplified symmetric problem (2.27)–(2.29). To do this, we expand variables in powers of ε,

$$z = z_0 + \varepsilon z_1 + \varepsilon^2 z_2 + \mathcal{O}(\varepsilon^3), \tag{3.1a}$$

$$m = m_0 + \varepsilon m_1 + \varepsilon^2 m_2 + \mathcal{O}(\varepsilon^3), \tag{3.1b}$$

$$\lambda = \lambda_0 + \varepsilon \lambda_1 + \varepsilon^2 \lambda_2 + \mathcal{O}(\varepsilon^3), \tag{3.1c}$$

$$\mu = \mu_0 + \varepsilon \mu_1 + \varepsilon^2 \mu_2 + \mathcal{O}(\varepsilon^3), \tag{3.1d}$$

$$\sigma = \sigma_0 + \varepsilon \sigma_1 + \varepsilon^2 \sigma_2 + \mathcal{O}(\varepsilon^3), \tag{3.1e}$$

$$J = J_0 + \varepsilon J_1 + \varepsilon^2 J_2 + \mathcal{O}(\varepsilon^3), \tag{3.1f}$$

as $\varepsilon \to 0$. On substituting these asymptotic series into (2.27)–(2.29), the leading-order solution is the evolution of two rigid filaments with infinite resistance to bending. The first-order corrections describe how small, non-zero bending affects the dynamics. In subsequent subsections, we present the key results and arguments, and give full details of the computations in Appendix B.

3.1 Ansatz For Rigid Filaments

We obtain an ansatz for the leading-order solution for rigid filaments from the $\mathcal{O}(1/\varepsilon)$ problem. On substituting the asymptotic expansions (3.1) into the simplified model (2.27)–(2.29), at $\mathcal{O}(1/\varepsilon)$ we obtain

$$z_0'''' = 0, \quad z_0'''|_{s=0,1} = 0, \quad z_0''|_{s=0,1} = 0, \quad |z_0'| = 1. \tag{3.2}$$

The solution to (3.2) for z_0 is a straight filament, whose direction we parameterise by the filament angle, $\theta/2$, measured from the positive vertical axis (see Figure 3.1) writing

$$z_0' = \begin{bmatrix} \sin(\theta/2) \\ \cos(\theta/2) \end{bmatrix}. \tag{3.3}$$

Note that for the orthogonal direction we use the notation

$$z_0'^{\perp} = \begin{bmatrix} -\cos(\theta/2) \\ \sin(\theta/2) \end{bmatrix}, \tag{3.4}$$

12

where the symbol $^{\perp}$ denotes the rotation to the left by $\pi/2$. A suitable ansatz for the position of a rigid filament solution satisfying the constraint (2.29b) is then

$$z_0 = \begin{pmatrix} 0 \\ y_0 \end{pmatrix} + z_0' \left(s - m_0 \right), \qquad (3.5)$$

158 where the leading-order motor relative position, m_0, and leading-order vertical position
159 of the intersection, y_0, complete the parameterisation. This situation is illustrated in
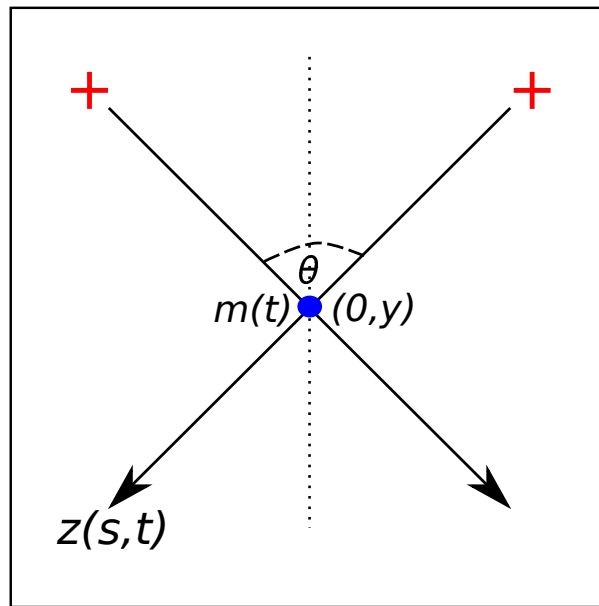Figure 3.1.

Figure 3.1: Schematic of the simplified two-filament-motor system with two rigid, symmetric actin filaments. The myosin motor has relative position $m(t)$, and physical position $(0, y(t))$. The two filaments are symmetric about the dashed vertical line, which is the positive y-axis. The angle between the filaments is θ, such that the angle between a filament and the y-axis is $\theta/2$.

160

3.2 Leading-Order Solution

To obtain the leading-order solution, we consider the $\mathcal{O}(1)$ problem

$$
\begin{cases}
\dfrac{\partial z_0}{\partial t} + z_1'''' - (\lambda_0 z_0')' + \mu_0 \begin{pmatrix} 1 \\ 0 \end{pmatrix} \delta\left(s - m_0\right) = 0, & \text{(3.6a)} \\[2ex]
0 = 1 - \mu_0 \sin\left(\dfrac{\theta}{2}\right), & \text{(3.6b)} \\[2ex]
z_1''' - \lambda_0 z_0'|_{s=0,1} = 0, & \text{(3.6c)} \\[2ex]
z_0\left(m_0(t), t\right) = \begin{pmatrix} 0 \\ y_0(t) \end{pmatrix}, & \text{(3.6d)} \\[2ex]
z_0' \cdot z_1' = 0. & \text{(3.6e)}
\end{cases}
$$

To proceed, we use the orthogonality condition (3.6e) to infer the ansatz

$$
z_1'(s, t) = h'(s, t) z_0'^{\perp}, \tag{3.7}
$$

where $h(s, t)$ is an arbitrary scalar function. Substituting (3.5) and (3.7) into (3.6a) enables us to solve for the leading-order quantities

$$
\mu_0 = \frac{1}{\sin(\theta/2)}, \quad \lambda_0 = H\left(s - m_0\right) - s, \quad \text{and} \quad \sigma_0 = 2\nu_0, \tag{3.8}
$$

where H is the Heaviside step function, and $\nu_0 = m_0 - 1/2$. Filament evolution then satisfies the ordinary differential equations

$$
\frac{\mathrm{d}S}{\mathrm{d}t} = -24\nu_0\left(1 - S\right), \tag{3.9a}
$$

$$
S\frac{\mathrm{d}\nu_0}{\mathrm{d}t} = 1 + 12\nu_0^2\left(1 - S\right), \tag{3.9b}
$$

where $S = \sin^2(\theta/2)$. Since z_0 is written in terms of the angle θ only, the system (3.9) determines z_0, and since h' is known, we subsequently obtain z_1. Full details on this calculation are available in Appendix B.

An important property of the system (3.9) is that it is invariant under a change of variables which reverses the direction of time. If we introduce the reversed-time $\tilde{t} = T - t$ for an arbitrary constant T, we have $\tilde{\nu}_0(\tilde{t}) = -\nu_0(T - \tilde{t})$ and $\tilde{\theta}(\tilde{t}) = \theta(T - \tilde{t})$ (*i.e.* $\tilde{S} = S$). Consequently, if the motor is initially positioned at the pointed ends ($\nu_0(0) = -1/2$), and

T denotes the time it reaches the barbed ends, then the time-aggregated stress vanishes,

$$
\begin{aligned}
J(T) - J(0) &= \int_0^{T/2} \sigma(t)\,\mathrm{d}t + \int_{T/2}^{T} \sigma(t)\,\mathrm{d}t, \\
&= \int_0^{T/2} 2\nu_0(t)\,\mathrm{d}t + \int_0^{T/2} 2\nu_0(T - \tilde{t})\,\mathrm{d}\tilde{t} \\
&= \int_0^{T/2} 2\nu_0\,\mathrm{d}t - \int_0^{T/2} 2\tilde{\nu}_0\,\mathrm{d}\tilde{t} = 0.
\end{aligned} \tag{3.10}
$$

This is because the equations and initial conditions satisfied by ν_0, θ, and $\tilde{\nu}_0$, $\tilde{\theta}$ both coincide, and we have that $\nu_0(\hat{t}) = \tilde{\nu}_0(\hat{t})$ for all $\hat{t} \in [0, T]$ (see also numerical result shown in Figure 4.1c). These results agree with the previously reported results (Dasanayake, Michalski, and Carlsson 2011; Lenz 2014) that rigid filaments with polarity-reversal symmetry produce zero net stress.

3.3   First-Order Corrections

The higher-order correction terms, z_1, σ_1 and J_1, elucidate the effect of small, non-zero bending on filament evolution and stress. To solve for these terms, we substitute the asymptotic expansions (3.1) into (2.30) and (2.31) to obtain

$$
\sigma = -2 \int_0^1 \lambda_0\,\mathrm{d}s - 2\varepsilon \int_0^1 \left(|z_1''|^2 + \lambda_1 \right)\,\mathrm{d}s + \mathcal{O}\left(\varepsilon^2 \right), \tag{3.11a}
$$

$$
J = \int_0^1 |z_0|^2\,\mathrm{d}s + 2\varepsilon \int_0^1 z_0 \cdot z_1\,\mathrm{d}s + \mathcal{O}\left(\varepsilon^2 \right). \tag{3.11b}
$$

Matching coefficients of ε then yields

$$
\sigma_1 = -2 \int_0^1 \left(|z_1''|^2 + \lambda_1 \right)\,\mathrm{d}s, \quad J_1 = 2 \int_0^1 z_0 \cdot z_1\,\mathrm{d}s. \tag{3.12}
$$

In addition, we use the PDE (3.6a) and the ansatz (3.7) to obtain an explicit expression for the curvature of z_1,

$$
h'' = -\cot\left(\frac{\theta}{2} \right) \left[(m_0 - s)H(s - m_0) + s^2(m_0(2s - 3) - s + 2) \right]. \tag{3.13}
$$

15

Since the first-order correction to stress, σ_1, involves the currently unknown λ_1, progress requires consideration of the $\mathcal{O}(\varepsilon)$ problem, which is

$$
\begin{cases}
\dfrac{\partial z_1}{\partial t} + z_2'''' - (\lambda_0 z_1' + \lambda_1 z_0')' + \mu_1 \begin{pmatrix} 1 \\ 0 \end{pmatrix} \delta\left(s - m_0\right) - \mu_0 \begin{pmatrix} 1 \\ 0 \end{pmatrix} \delta'\left(s - m_0\right) m_1 = 0, & \text{(3.14a)} \\[3mm]
0 = - \begin{pmatrix} 1 \\ 0 \end{pmatrix} \left(\mu_1 z_0'(m_0(t), t) + \mu_0 z_1'(m_0(t), t)\right), & \text{(3.14b)} \\[3mm]
z_2''' - \lambda_0 z_1' - \lambda_1 z_0'|_{s=0,1} = 0, & \text{(3.14c)} \\[2mm]
z_2''|_{s=0,1} = 0, & \text{(3.14d)} \\[2mm]
z_1\left(m_0(t), t\right) + z_0'(m_1(t), t) = \begin{pmatrix} 0 \\ y_1(t) \end{pmatrix}, & \text{(3.14e)} \\[3mm]
|z_1'|^2 + 2 z_0' \cdot z_2' = 0. & \text{(3.14f)}
\end{cases}
$$

Obtaining the solution to (3.14) involves an intricate calculation based on the ansatz

$$
z_1 = \begin{pmatrix} 0 \\ y_1(t) \end{pmatrix} - z_0'(t) m_1 + z_0'^{\perp} \left[A(t)(s - m_0) + \int_{m_0}^{s} \tilde{h}'(s, t)\, \mathrm{d}s\right], \qquad (3.15)
$$

which reflects (3.14e) and (3.7). This gives rise to a system of equations for the degrees of freedom $A(t)$, $y_1(t)$, and $m_1(t)$. We provide full details on the calculation to obtain this in Appendix B. A key result is the stress correction term,

$$
\sigma_1 = -2 \int_0^1 |h''|^2 \, \mathrm{d}s - 2 \left[A + \tilde{h}'(m_0, t)\right] \cot\left(\frac{\theta}{2}\right)\left(\frac{1}{2} - m_0\right) + 2 m_1, \qquad (3.16)
$$

where $\tilde{h}'(m_0, t)$ is given by

$$
\tilde{h}'(m_0, t) = -\frac{1}{12} m_0^3 \left(6 m_0^2 - 15 m_0 + 8\right) \cot\left(\frac{\theta}{2}\right). \qquad (3.17)
$$

Similar to the system (3.9), we can obtain a system of differential equations to solve for $A(t)$, $y_1(t)$, and $m_1(t)$. Since h'' and $\tilde{h}'$ are in terms of the leading-order degrees of freedom θ and m_0, we can subsequently compute σ_1. However, the ODEs for $A(t)$, $y_1(t)$, and $m_1(t)$ have no exact solution. Therefore, we continue our investigation using numerical solutions.

4 Numerical Solutions

We compute numerical solutions to the simplified system (2.27) in JULIA, by constructing a dimensionless version of the functional (2.2), and using `Optim.jl` (Mogensen and Risbeth 2018) to obtain the minimiser at each time step. This is equivalent to a time-implicit

numerical method for solving (2.22). We represent filaments as 50 equal-length line segments joined at nodes, about which segments can rotate. Each filament has total length $1\,\mu m$ (Kamasaki, Osumi, and Mabuchi 2007), and we solve the model using the time step size $\Delta t = 0.001$. We perform the minimisation using the limited-memory Broyden–Fletcher–Goldfarb–Shanno (LBFGS) method and incorporate automatic differentiation (`ForwardDiff.jl`) to compute the gradient of the energy (2.2).

4.1 Comparison With Asymptotic Analysis

We begin by computing numerical solutions for two symmetric filaments with $m(0) = 0$, and $\theta(0) = \pi/2$. Like the asymptotic analysis, we assume these filaments are initially rigid, $V_m \to \infty$, and solve until the motor reaches the plus-end and detaches. First, we compute a solution for two rigid ($\varepsilon = 1 \times 10^{-5}$) filaments, to validate the leading-order bulk stress $\sigma_0 = 2\nu_0$, and the solution to (3.9) which governs z_0. As Figures 4.1a and 4.1b show, for both of these we obtain agreement between the numerical solution and leading-order solution. Furthermore, Figure 4.1c illustrates the result from (3.10), namely that zero net stress is generated when a motor traverses two rigid filaments from the minus to plus-ends, *i.e.* $J_0(T) = J_0(0) = 0$, where $T = 0.627$ is the time at which the motor reaches the plus end.

Next, we solve the model with $\varepsilon = 0.01$ to validate the formulae for h'' and σ_1, (3.13) and (3.16) respectively. The dynamics of the two filaments and motor are illustrated in Figure 4.2. As part of the solution, we compute h'' using the asymptotic formula (3.13) and numerical values of θ and m, and compare this with the numerical value for the curvature,

$$h'' = \frac{1}{\varepsilon} \left(z_0'^{\perp} \cdot z'' \right). \tag{4.1}$$

This comparison is shown in Figure 4.3. At each time step, we obtain agreement between the numerical and asymptotic results. The curvature formula (3.13) also reveals the shape that the two filaments adopt as they evolve (the qualitative pattern is easier to see in Figure 4.6). Initially, the filaments adopt a convex shape, as the positive curvature in Figure 4.3a shows. As the motor moves and pulls the filaments inwards, their shape changes to concave, as Figures 4.3c and 4.3d show. When the motor approaches the plus-end, the filaments return to a convex shape. The asymptotic result for h'' remains accurate for up to $\varepsilon \sim \mathcal{O}(1)$, before breaking down for $\varepsilon \sim \mathcal{O}(10)$.

We also use the numerical solution with $\varepsilon = 0.01$ to validate the formula for σ_1, the first-order correction to bulk stress. At each time step, we compute the stress σ, and compare with the stress in a simulation with $\varepsilon = 1 \times 10^{-4}$, which we consider to be σ_0 for rigid filaments. We then approximate the first-order correction as $\sigma_1 \approx (\sigma - \sigma_0)/\varepsilon$, and present results in Figure 4.4a. For most values of t, it holds that $\sigma_1 > 0$. In particular, larger positive values of σ_1 occur close to $t = 0$ and $t = T$, or $m = 0$ and $m = 1$.

17
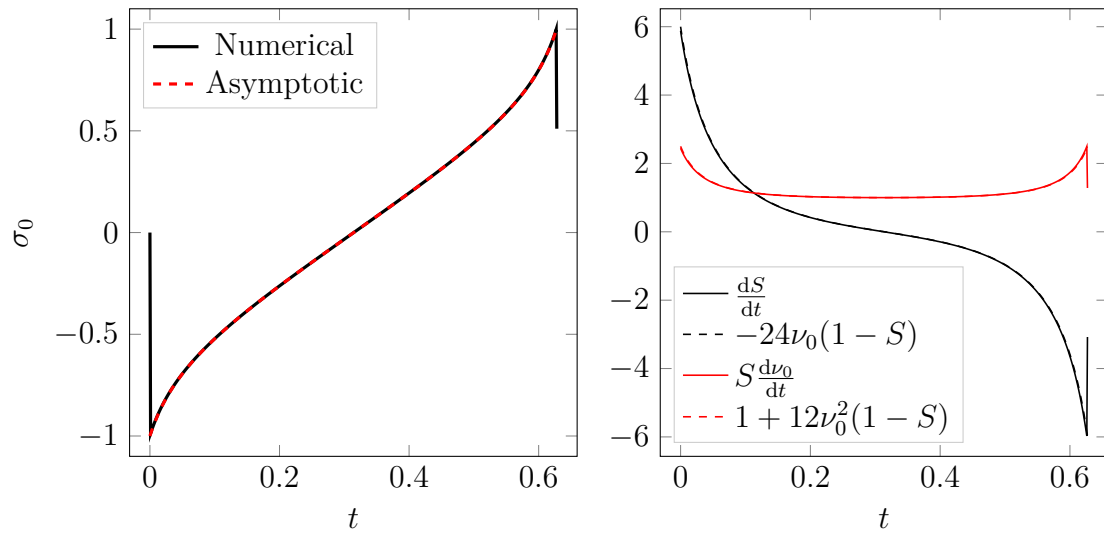
(a) Leading-order bulk stress, σ_0.

(b) System of ODEs, (3.9).
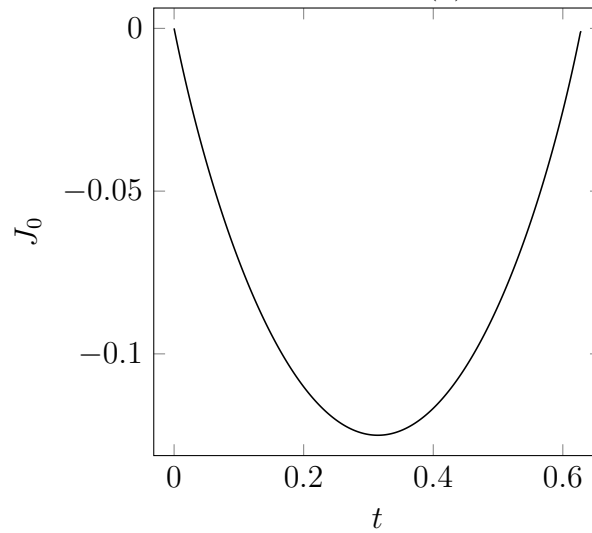
(c) J_0

Figure 4.1: Comparison between a numerical solution with rigid filaments ($\varepsilon = 1 \times 10^{-5}$) and the leading-order asymptotic solution.
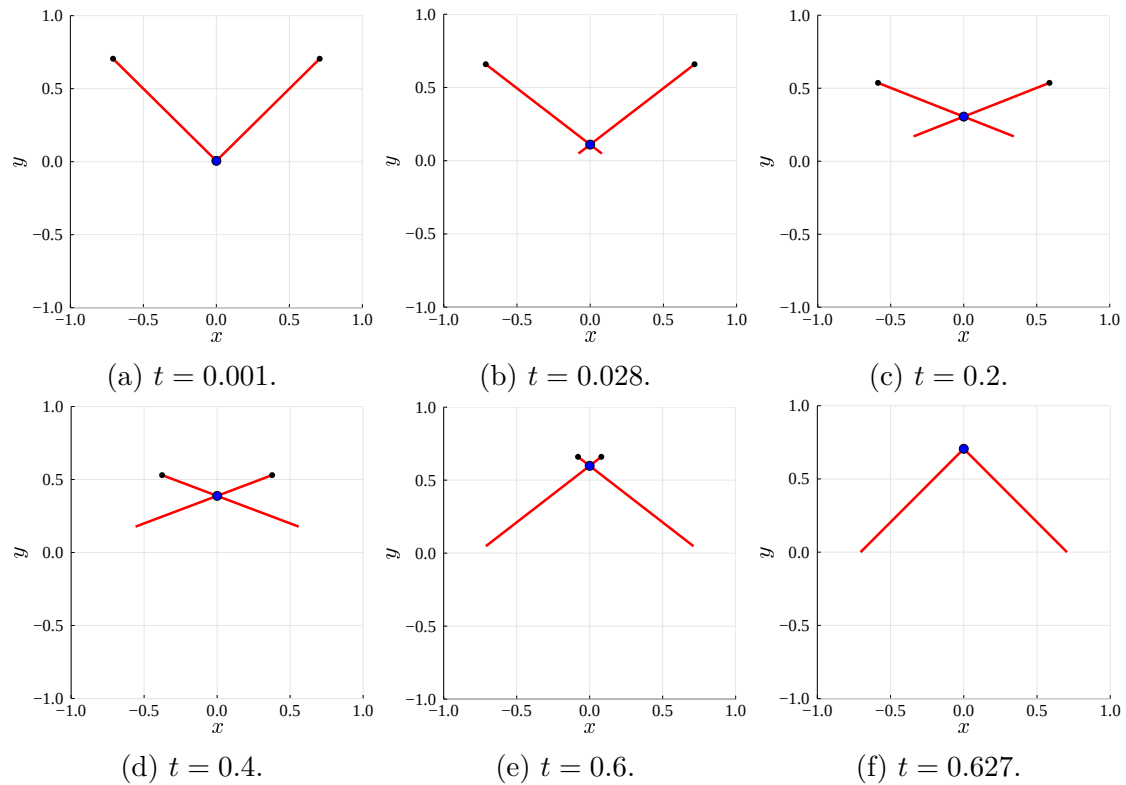
Figure 4.2: Numerical solution for the evolution of two actin filaments (red solid curves) with $\varepsilon = 0.01$. The black nodes indicate the filament plus ends, and the blue dot at the filament intersection represents the myosin motor.

Figure 4.4a is surprising, because it suggests the introduction of filament bending generates stresses that are biased to expansion. Similarly, as Figure 4.4b shows, the quantity $J_1(T) - J_1(0) > 0$, also suggesting net expansive bias. Based on this, one might conclude that bending cannot facilitate microscopic-scale contraction. However, we have not yet accounted for the changes in filament geometry, and how they influence motor dynamics. Further simulations in §4.2 will reveal this more clearly, and confirm that bending does facilitate net microscopic-scale contraction.

4.2 Symmetric Flexible Filaments

We now consider numerical solutions beyond the $\varepsilon \ll 1$ regime considered in the asymptotic analysis. These solutions are with the same conditions as Figure 4.2, where the motor is initially at the minus-ends of two symmetric filaments. We then solve the model until the motor reaches the plus-ends. Results are presented in Figure 4.5. The quantity $J(t)$ measures the effect of ε on net stress. This is shown in Figure 4.5a. For rigid filaments, we showed that $J(T) - J(0) = 0$, indicating zero net stress as the motor moved from the minus to the plus-ends. Since $J(T)$ decreases as ε increases, the introduction of filament bending facilitates bias to contraction. This is despite the quantities $\sigma_1(T)$ and $J_1(T)$ being positive, as in Figure 4.4a and 4.4b. Indeed, Figure 4.5b confirms that $\sigma_1 > 0$, with
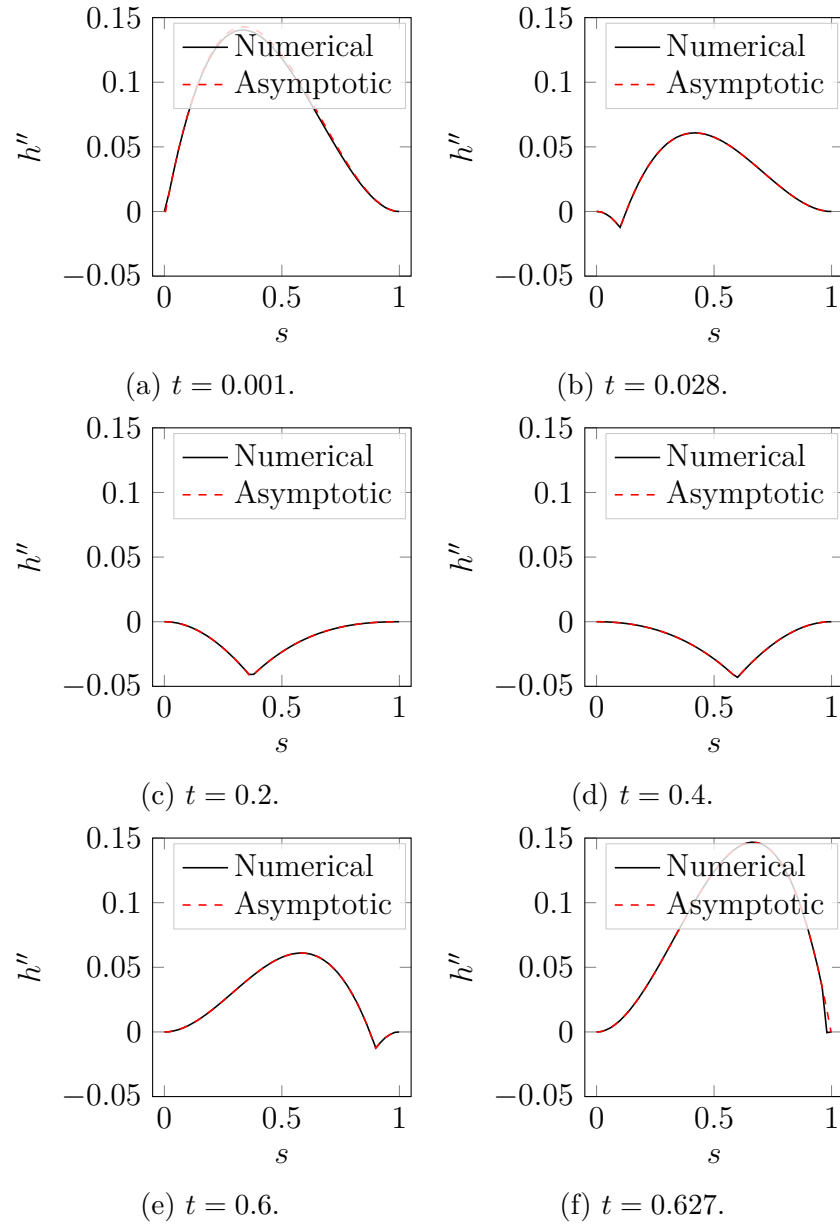
Figure 4.3: Numerical and asymptotic solutions for $h''(s,t)$, the curvature of z_1, in a numerical solution with $\varepsilon = 0.01$, and $\theta(0) = \pi/2$.
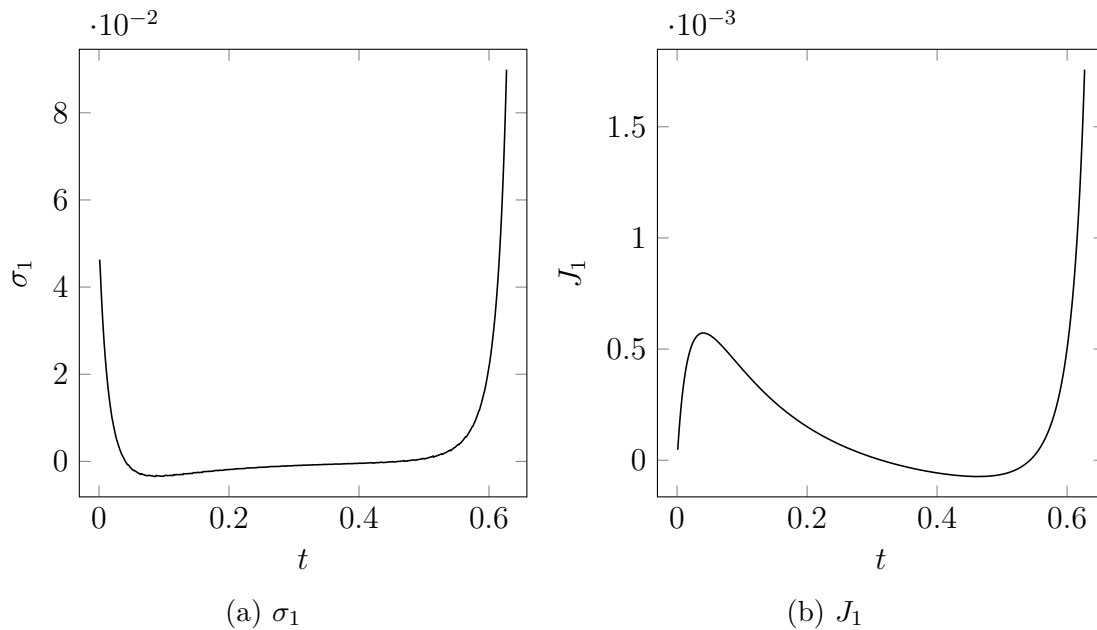
(a) σ_1 (b) J_1

Figure 4.4: Calculation of $\sigma_1 \approx (\sigma - \sigma_0)/\varepsilon$ and $J_1 \approx (J - J_0)/\varepsilon$ in the numerical solution with $\varepsilon = 0.01$. The values of σ_0 and J_0 were obtained using a solution with $\varepsilon = 1 \times 10^{-4}$.

stress increasing with ε close to $t = 0$ and $t = T$.

Semi-flexible filaments facilitates net contraction because bending breaks the polarity-reversal symmetry, and the resulting geometry favours contraction. As Figure 4.5c shows, with increasing ε, the myosin motor moves faster along the filaments and detaches earlier. The increase in motor speed is largest as the motor approaches the plus-ends, which Figure 4.5b shows is associated with expansion. As the motor approaches the plus-ends, the semi-flexible filaments adopt a convex shape that brings them closer to parallel at their tips, as illustrated in Figure 4.5d. This decreases the spring force through the motor, enabling it to move faster. Since the motor moves faster close to the plus-ends, the expansive component persists for shorter time than the contractile component. Consequently, the time-integrated stress $J(T) - J(0)$ decreases as ε increases.

The results in Figure 4.5 are relevant for *in vivo* actin filaments, for which the parameters (Kamasaki, Osumi, and Mabuchi 2007; Gittes et al. 1993; Thoresen, Lenz, and Gardel 2011; Reichl et al. 2008; Oelz, Rubinstein, and Mogilner 2015) estimated in Tam, Mogilner, and Oelz (2021) give $\varepsilon = 68.5$. To further our analysis, we compute a numerical solution with $\varepsilon = 68.5$ and $V_m = 1$, to investigate whether contraction persists after relaxing the assumption of infinite motor velocity. The evolution of these filaments is shown in Figure 4.6. Despite the slower motor speed, the evolution qualitatively follows the prediction from Figure 4.3. Filaments are initially convex, then become concave, and adopt a convex shape again as the motor approaches the plus-ends. As Figure 4.6f shows, the two filaments are curved when the motor reaches the plus-ends and detaches. To rule out the possibility that relaxation to straight configuration produces expansion that cancels out net contraction, we continued the simulation after motor detachment, until the
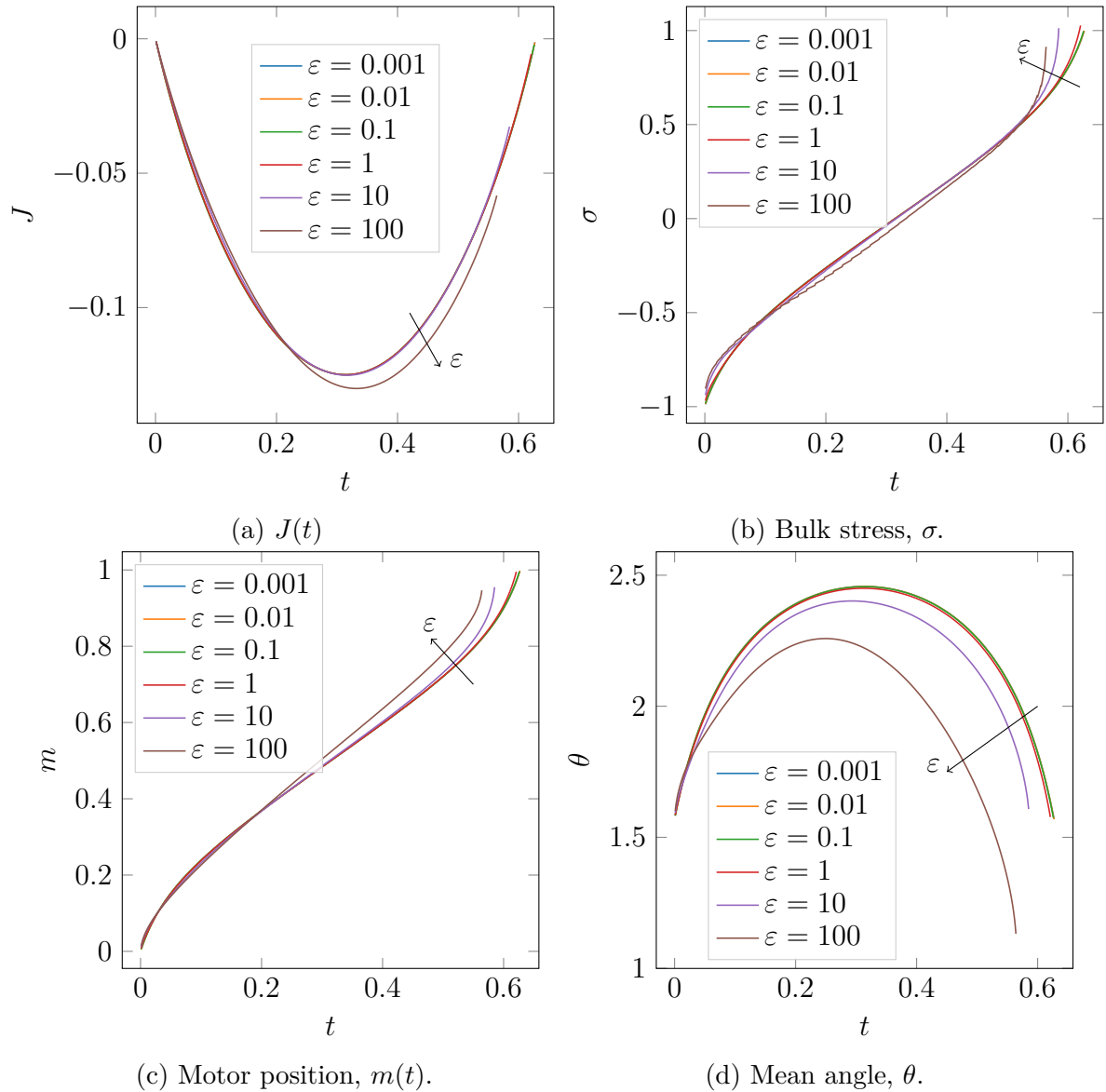
21

(a) $J(t)$

(b) Bulk stress, σ.

(c) Motor position, $m(t)$.

(d) Mean angle, θ.

Figure 4.5: The effect of ε on relevant quantities in solutions of two symmetric filaments. Solutions are computed with $m(0) = 0$, $\theta(0) = \pi/2$, and proceed for all $t \in [0, T(\varepsilon)]$ such that $m(t) < 1$. After this time T, the motor reaches the plus-end and detaches. Results are plotted for six values of ε, and arrows indicate the direction of increasing ε.

(a) $t = 0$.   (b) $t = 0.3$.   (c) $t = 0.6$.

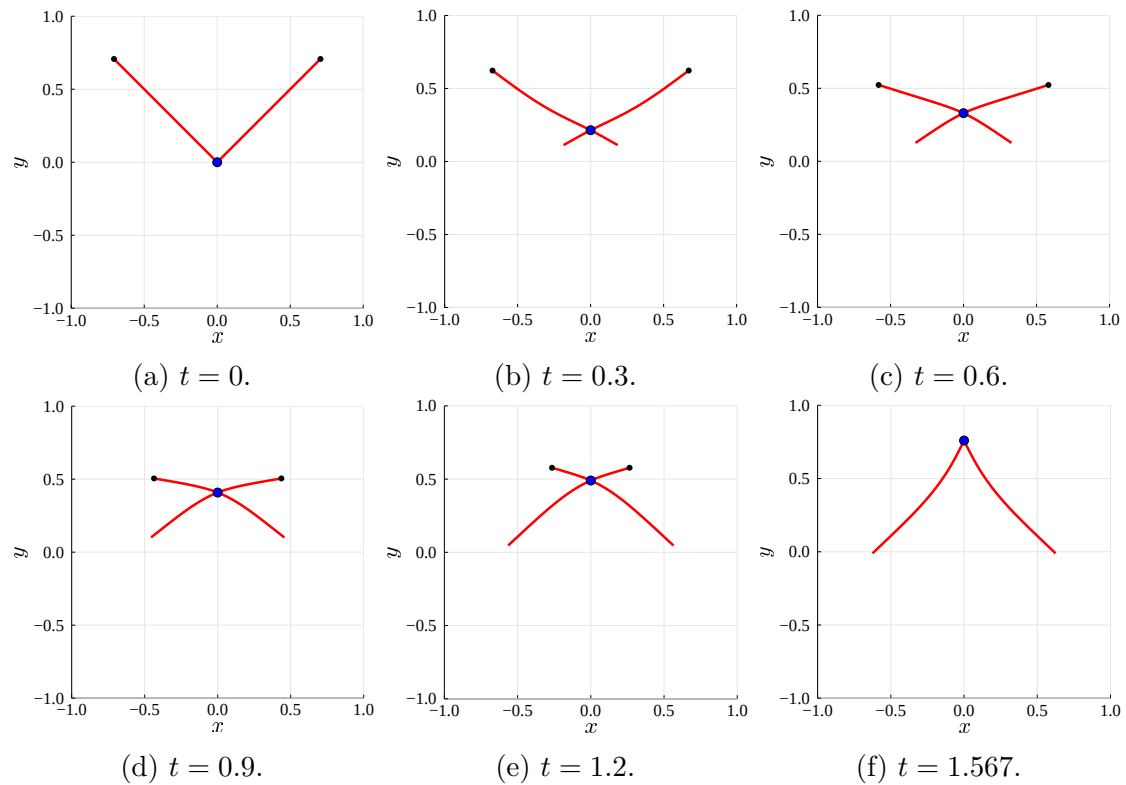(d) $t = 0.9$.   (e) $t = 1.2$.   (f) $t = 1.567$.

Figure 4.6: Numerical solution for the evolution of two flexible actin filaments (red solid curves) with $\varepsilon = 68.5$ and $V_m = 1$. The black nodes indicate the filament plus ends, and the blue dot at the filament intersection represents the myosin motor.

filaments were again straight. We plot $\sigma(t)$ and $J(t)$ in Figure 4.7. Although relaxation to the straight configuration (shown in Figure 4.7a) generates a small amount of expansive stress, Figure 4.7c shows $J(2) - J(0) < 0$, suggesting net contraction. Thus, our proposed geometric mechanism for contraction remains relevant for realistic filament flexural rigidity and motor speed. Since actomyosin networks (for example those in the cortex) consist of many cross-linked two-filament assemblies, our mechanism provides a possible explanation for the microscopic origin of network-scale actomyosin contraction.

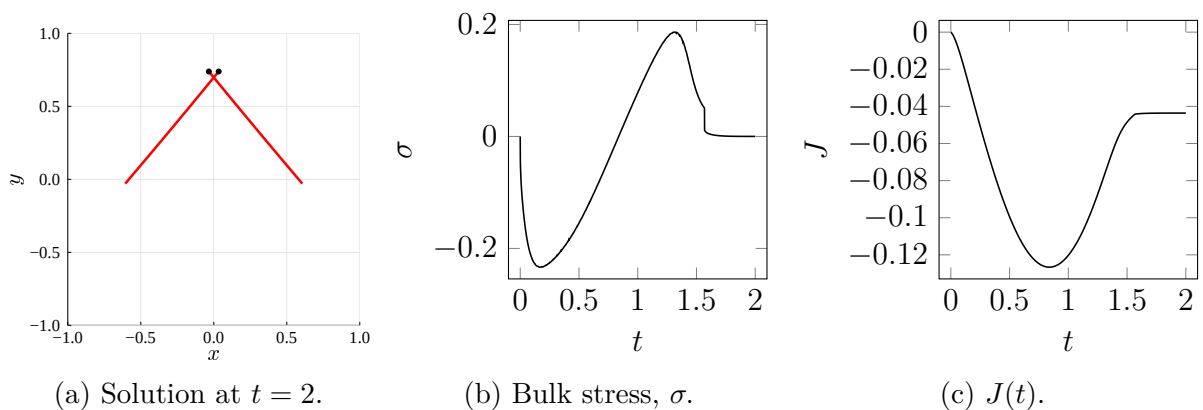(a) Solution at $t = 2$.   (b) Bulk stress, σ.   (c) $J(t)$.

Figure 4.7: The final filament configuration, bulk stress, σ, and $J(t)$ for the flexible filament ($\varepsilon = 68.5$ and $V_m = 1$) solution in Figure 4.6.

256

23

5   Conclusion

Understanding the origins of actomyosin contraction is an open problem in cellular biophysics, with implications for cell movement and division. In this paper, we presented a detailed investigation of how two a two-filament-motor system generates microscopic contraction if the filaments are flexible. We first derived a partial differential equation model, and described a method of computing in-plane stress. We then applied asymptotic analysis to a symmetric system with infinite free-moving motor velocity. The leading-order solution showed that two rigid filaments do not generate net stress if the motor traverses the entire length of the filaments. However, the introduction of filament bending enables the two-filament structure to generate net contraction. This is because bending breaks the polarity-reversal symmetry of rigid filaments. The resulting geometric asymmetry draws the plus-ends closer to parallel as the motor approaches. This facilitates faster motor movement when motors are close to filament plus-ends, and inhibits production of expansive stress.

Our analysis confirms that the microscopic dynamics of symmetric filament pairs and motors can explain contraction. We expect that the same mechanism also favours contraction in non-symmetric fibre-motor assemblies and that, consequently, macroscopic contraction in disordered networks could arise from the accumulation of multiple filament pairs, without the need for nonlinear amplification of contractile stress. Nevertheless, the question of how these results apply to networks, in which filaments cross at arbitrary angle and position, remains open. In Tam, Mogilner, and Oelz (2021) it has been confirmed that such networks relying on the biomechanical model for semi-flexible fibres and motors presented in this study do contract. We also mention that another potential approach is to derive a coarse-grained, continuum model based on the assumption of infinite filament length (Oelz 2014). This, and understanding how these microscopic mechanics give rise to structures including stress fibres (Pellegrin and Mellor 2007) and the contractile ring (Kamasaki, Osumi, and Mabuchi 2007; Svitkina 2018), will be subjects of future work.

Acknowledgements

Declaration

The authors have no conflicts of interest to declare.

References

Belmonte, J. M., M. Leptin, and F. J. Nédélec (2017), "A theory that predicts behaviors of disordered cytoskeletal networks", *Molecular Systems Biology* 13, 941, DOI: 10.15252/msb.20177796.

Bidone, T. C., W. Jung, D. Maruri, C. Borau, R. D. Kamm, and T. Kim (2017), "Morphological transformation and force generation of active cytoskeletal networks", *PLoS Computational Biology* 13, e1005277, DOI: 10.1371/journal.pcbi.1005277.

Bormuth, V., V. Varga, J. Howard, and E. Schäffer (2009), "Protein friction limits diffusive and directed movements of kinesin motors in microtubules", *Science* 325, pp. 870–873, DOI: 10.1126/science.1174923.

Broedersz, C. P. and F. C. Mackintosh (2014), "Modeling semiflexible polymer networks", *Reviews of Modern Physics* 86, pp. 995–1036, DOI: 10.1103/RevModPhys.86.995.

Chalut, K. J. and E. K. Paluch (2016), "The actin cortex: a bridge between cell shape and function", *Developmental Cell* 38, pp. 571–573, DOI: 10.1016/j.devcel.2016.09.011.

Cheffings, T. H., N. J. Burroughs, and M. K. Balasubramanian (2016), "Actomyosin ring formation and tension generation in eukaryotic cytokinesis", *Current Biology* 26, R719–R739, DOI: 10.1016/j.cub.2016.06.071.

Dasanayake, N. L., P. J. Michalski, and A. E. Carlsson (2011), "General mechanism of actomyosin contractility", *Physical Review Letters* 107, 118101, DOI: 10.1103/PhysRevLett.107.118101.

De La Cruz, E. M. and M. L. Gardel (2015), "Actin mechanics and fragmentation", *Journal of Biological Chemistry* 290, pp. 17137–17144, DOI: 10.1074/jbc.R115.636472.

du Roure, O., A. Lindner, E. N. Nazockdast, and M. J. Shelley (2019), "Dynamics of flexible fibers in viscous flows and fluids", *Annual Review of Fluid Mechanics* 51, pp. 539–572, DOI: 10.1146/annurev-fluid-122316-045153.

Ennomani, H., G. Letort, C. Guérin, J. Martiel, W. Cao, F. J. Nédélec, E. M. De La Cruz, M. Théry, and L. Blanchoin (2016), "Architecture and connectivity govern actin network contractility", *Current Biology* 26, pp. 616–626, DOI: 10.1016/j.cub.2015.12.069.

Freedman, S. L., S. Banerjee, G. M. Hocky, and A. R. Dinner (2017), "A versatile framework for simulating the dynamic mechanical structure of cytoskeletal networks", *Biophysical Journal* 113, pp. 448–460, DOI: 10.1016/j.bpj.2017.06.003.

Freedman, S. L., G. M. Hocky, S. Banerjee, and A. R. Dinner (2018), "Nonequilibrium phase diagrams for actomyosin networks", *Soft Matter* 14, pp. 7740–7747, DOI: 10.1039/c8sm00741a.

Gautel, M. (2011), "The sarcomeric cytoskeleton: who picks up the strain?", *Current Opinion in Cell Biology* 23, pp. 39–46, DOI: 10.1016/j.ceb.2010.12.001.

Gittes, F., B. Mickey, J. Nettleton, and J. Howard (1993), "Flexural rigidity of microtubules and actin filaments measured from thermal fluctuations in shape", *Journal of Cell Biology* 120, pp. 923–934, DOI: `10.1083/jcb.120.4.923`.

Head, D. A., A. J. Levine, and F. C. MacKintosh (2003), "Distinct regimes of elastic response and deformation modes of cross-linked cytoskeletal and semiflexible polymer networks", *Physical Review E* 68, 061907, DOI: `10.1103/PhysRevE.68.061907`.

Hiraiwa, T. and G. Salbreux (2016), "Role of turnover in active stress generation in a filament network", *Physical Review Letters* 116, 188101, DOI: `10.1103/PhysRevLett.116.188101`.

Huxley, H. E. (2004), "Fifty years of muscle and the sliding filament hypothesis", *European Journal of Biochemistry* 271, pp. 1403–1415, DOI: `10.1111/j.1432-1033.2004.04044.x`.

Kamasaki, T., M. Osumi, and I. Mabuchi (2007), "Three-dimensional arrangement of F-actin in the contractile ring of fission yeast", *Journal of Cell Biology* 178, pp. 765–771, DOI: `10.1083/jcb.200612018`.

Kim, T. (2015), "Determinants of contractile forces generated in disorganized actomyosin bundles", *Biomechanics and Modeling in Mechanobiology* 14, pp. 345–355, DOI: `10.1007/s10237-014-0608-2`.

Komianos, J. E. and G. A. Papoian (2018), "Stochastic ratcheting on a funneled energy landscape is necessary for highly efficient contractility of actomyosin force diploes", *Physical Review X* 8, 021006, DOI: `10.1103/PhysRevX.8.021006`.

Langer, J. and D. A. Singer (1984), "Knotted elastic curves in $\mathbb{R}^3$", *Journal of the London Mathematical Society* 30, pp. 512–520, DOI: `10.1112/jlms/s2-30.3.512`.

— (1987), "Curve-straightening in Riemannian manifolds", *Annals of Global Analysis and Geometry* 5, pp. 133–150, DOI: `10.1007/BF00127856`.

Lenz, M. (2014), "Geometrical origins of contractility in disordered actomyosin networks", *Physical Review X* 4, 041002, DOI: `10.1103/PhysRevX.4.041002`.

— (2020), "Reversal of contractility as a signature of self-organization in cytoskeletal bundles", *eLife* 9, e51751, DOI: `10.7554/eLife.51751`.

Lenz, M., T. Thoresen, M. L. Gardel, and A. R. Dinner (2012), "Contractile units in disordered actomyosin bundles arise from F-actin buckling", *Physical Review Letters* 108, 238107, DOI: `10.1103/PhysRevLett.108.238107`.

Letort, G., A. Z. Politi, H. Ennomani, M. Théry, F. J. Nédélec, and L. Blanchoin (2015), "Geometrical and mechanical properties control actin filament organization", *PLoS Computational Biology* 11, e1004245, DOI: `10.1371/journal.pcbi.1004245`.

Linnér, A. (1989), "Some properties of the curve straightening flow in the plane", *Transactions of the Americal Mathematical Society* 314, pp. 605–617, DOI: `10.1090/s0002-9947-1989-0989580-5`.

363 Linnér, A. (2003), "Symmetrized curve-straightening", *Differential Geometry and its*
364 *Applications* 18, pp. 119–146, DOI: 10.1016/S0926-2245(02)00144-4.

365 McFadden, W. M., P. M. McCall, M. L. Gardel, and E. M. Munro (2017), "Filament
366 turnover tunes both force generation and dissipation to control long-range flows in a
367 model actomyosin cortex", *PLoS Computational Biology* 13, e1005811, DOI: 10.1371/
368 journal.pcbi.1005811.

369 Mogensen, P. K. and A. N. Risbeth (2018), "Optim: A mathematical optimization package
370 for Julia", *Journal of Open Source Software* 3, 615, DOI: 10.21105/joss.00615.

371 Murrell, M. P. and M. L. Gardel (2012), "F-actin buckling coordinates contractility and
372 severing in biomimetic actomyosin cortex", *Proceedings of the National Academy of*
373 *Science of the United States of America* 109, pp. 20820–20825, DOI: 10.1073/pnas.
374 1214753109.

375 Murrell, M. P., P. W. Oakes, M. Lenz, and M. L. Gardel (2015), "Forcing cells into shape:
376 the mechanics of actomyosin contractility", *Nature Reviews Molecular Cell Biology* 16,
377 pp. 486–498, DOI: 10.1038/nrm4012.

378 Oelz, D. B. (2011), "On the curve straightening flow of inextensible, open, planar curves",
379 *SeMA Journal: Bulletin of the Spanish Society of Applied Mathematics* 54, pp. 5–24,
380 DOI: 10.1007/BF03322585.

381 — (2014), "A viscous two-phase model for contractile actomyosin bundles", *Journal of*
382 *Mathematical Biology* 68, pp. 1653–1676, DOI: 10.1007/s00285-013-0682-6.

383 Oelz, D. B., B. Y. Rubinstein, and A. Mogilner (2015), "A combination of actin treadmilling
384 and cross-linking drives contraction of random actomyosin arrays", *Biophysical Journal*
385 109, pp. 1818–1829, DOI: 10.1016/j.bpj.2015.09.013.

386 Pellegrin, S. and H. Mellor (2007), "Actin stress fibres", *Journal of Cell Science* 120,
387 pp. 3491–3499, DOI: 10.1242/jcs.018473.

388 Pollard, T. D. (2010), "Mechanics of cytokinesis in eukaryotes", *Current Opinion in Cell*
389 *Biology* 22, pp. 50–56, DOI: 10.1016/j.ceb.2009.11.010.

390 Pollard, T. D. and B. O'Shaughnessy (2019), "Molecular mechanism of cytokinesis",
391 *Annual Review of Biochemistry* 88, pp. 661–689, DOI: 10.1146/annurev-biochem-
392 062917012530.

393 Popov, K., J. E. Komianos, and G. A. Papoian (2016), "MEDYAN: Mechanochemical
394 simulations of contraction and polarity alignment in actomyosin networks", *PLoS*
395 *Computational Biology* 12, e1004877, DOI: 10.1371/journal.pcbi.1004877.

396 Reichl, E. M., Y. Ren, M. K. Morphew, M. Delannoy, J. C. Effler, K. D. Girard, S. Divi,
397 P. A. Iglesias, S. C. Kuo, and D. N. Robinson (2008), "Interactions between myosin and
398 actin crosslinkers control cytokinesis contractility dynamics and mechanics", *Current*
399 *Biology* 18, pp. 471–480, DOI: 10.1016/j.cub.2008.02.056.

Ronceray, P., C. P. Broedersz, and M. Lenz (2016), "Fiber networks amplify active stress", *Proceedings of the National Academy of Science of the United States of America* 113, pp. 2827–2832, DOI: 10.1073/pnas.1514208113.

Soares e Silva, M., M. Depken, B. Stuhrmann, M. Korsten, F. C. MacKintosh, and G. H. Koenderink (2011), "Active multistage coarsening of actin networks driven by myosin motors", *Proceedings of the National Academy of Science of the United States of America* 108, pp. 9408–9413, DOI: 10.1073/pnas.1016616108.

Stachowiak, M. R., C. Laplante, H. F. Chin, B. Guirao, E. Karatekin, T. D. Pollard, and B. O'Shaughnessy (2014), "Mechanism of cytokinetic contractile ring constriction in fission yeast", *Developmental Cell* 29, pp. 547–561, DOI: 10.1016/j.devcel.2014.04.021.

Svitkina, T. M. (2018), "Ultrastructure of the actin cytoskeleton", *Current Opinion in Cell Biology* 54, pp. 1–8, DOI: 10.1016/j.ceb.2018.02.007.

Tam, A. K. Y., A. Mogilner, and D. B. Oelz (2021), "Protein friction and filament bending facilitate contraction of disordered actomyosin networks", *Biophysical Journal*, in press, DOI: https://doi.org/10.1016/j.bpj.2021.08.012.

Tawada, K. and K. Sekimoto (1991), "Protein friction exerted by motor enzymes through a weak-binding interaction", *Journal of Theoretical Biology* 150, pp. 193–200, DOI: 10.1016/S0022-5193(05)80331-5.

Thoresen, T., M. Lenz, and M. L. Gardel (2011), "Reconstitution of contractile actomyosin bundles", *Biophysical Journal* 100, pp. 2698–2705, DOI: 10.1016/j.bpj.2011.04.031.

Wen, Y. (1993), "L^2 flow of curve straightening in the plane", *Duke Mathematics Journal* 70, pp. 683–698, DOI: 10.1215/S0012-7094-93-07016-0.

— (1995), "Curve straightening flow deforms closed plane curves with nonzero rotation number to circles", *Journal of Differential Equations* 120, pp. 89–107, DOI: 10.1006/jdeq.1995.1106.

Yamada, K. M. and M. Sixt (2019), "Mechanisms of 3D cell migration", *Nature Reviews Molecular Cell Biology* 20, pp. 738–752, DOI: 10.1038/s41580-019-0172-9.

Yu, Q., J. Li, M. P. Murrell, and T. Kim (2018), "Balance between force generation and relaxation leads to pulsed contraction of actomyosin networks", *Biophysical Journal* 115, pp. 2003–2013, DOI: 10.1016/j.bpj.2018.10.008.

A   Mathematical Model Derivation

In this Appendix, we present a detailed derivation of the PDE model (2.14)–(2.16). We derive the system of force-balance PDEs using the variational principle. The energy functional for the structure consisting of a myosin motor attached to two semi-flexible actin filaments is

$$
\begin{aligned}
E[z_1, z_2, m_1, m_2] := & \sum_{i=1}^{2} \int_0^{L_i} \left(\frac{\lambda_a}{2\Delta t} |z_i - \boldsymbol{F} z_i^n|^2 + \frac{\kappa_a}{2} |z_i''|^2 + \frac{1}{\delta_a} \left(|z_i'| - 1 \right)^2 \right) \mathrm{d}s \\
& + \frac{1}{\delta_m} |z_1(m_1, t) - z_2(m_2, t)|^2 + \sum_{j=1}^{2} \left(-F_s m_j + \frac{F_s}{V_m} \frac{\left(m_j - m_j^n \right)^2}{2\Delta t} \right),
\end{aligned}
\tag{A.1}
$$

where $z_i(s, t) = (x_i(s, t), y_i(s, t))$, for $i = 1, 2$, are the filament shapes and positions, $m_1(t)$, and $m_2(t)$ are the motor relative positions, and

$$
\boldsymbol{F} = \begin{bmatrix} L_{xx}/L_{xx}^n & L_{yx}/L_{yy}^n \\ L_{xy}/L_{xx}^n & L_{yy}/L_{yy}^n \end{bmatrix}
\tag{A.2}
$$

is the deformation gradient tensor. According to the variational principle underlying the derivation, the solution at the next time step is such that the functional derivative with respect to all degrees of freedom vanishes, that is

$$
\frac{\delta E}{\delta z_1} = 0, \quad \frac{\delta E}{\delta z_2} = 0, \quad \frac{\delta E}{\delta m_1} = 0, \quad \text{and} \quad \frac{\delta E}{\delta m_2} = 0.
\tag{A.3}
$$

Evaluating each of (A.3) gives rise to the variational equations

$$
\begin{cases}
0 = \int_0^{L_1} \frac{\lambda_a}{\Delta t} \delta z_1 \cdot (z_1 - \boldsymbol{F} z_1^n) + \kappa_a z_1'' \cdot \delta z_1'' + & \text{(A.4a)} \\
\quad + \frac{2}{\delta_a} (|z_1'| - 1) \frac{z_1' \cdot \delta z_1'}{|z_1'|} \, \mathrm{d}s + \frac{2}{\delta_m} (z_1(m_1, t) - z_2(m_1, t)) \cdot \delta z_1 (m_1, t), & \text{(A.4b)} \\
0 = \int_0^{L_2} \frac{\lambda_a}{\Delta t} \delta z_2 \cdot (z_2 - \boldsymbol{F} z_2^n) + \kappa_a z_2'' \cdot \delta z_2'' + & \text{(A.4c)} \\
\quad + \frac{2}{\delta_a} (|z_2'| - 1) \frac{z_2' \cdot \delta z_2'}{|z_2'|} \, \mathrm{d}s - \frac{2}{\delta_m} (z_1(m_1, t) - z_2(m_1, t)) \cdot \delta z_2 (m_2, t), & \text{(A.4d)} \\
0 = \delta m_1 \left[-F_s + \frac{F_s}{V_m} \frac{(m_1 - m_1^n)}{\Delta t} + \frac{2}{\delta_m} (z_1(m_1, t) - z_2(m_1, t)) \cdot z_1' (m_1, t) \right], & \text{(A.4e)} \\
0 = \delta m_2 \left[-F_s + \frac{F_s}{V_m} \frac{(m_2 - m_2^n)}{\Delta t} - \frac{2}{\delta_m} (z_1(m_1, t) - z_2(m_1, t)) \cdot z_2' (m_2, t) \right]. & \text{(A.4f)}
\end{cases}
$$

For the motor evolution equations (A.4e) and (A.4f), we can immediately apply the continuum limit $\Delta t \to 0$, for which $\dot{m}_i = (m_i - m_i^n)/\Delta t$ for $i = 1, 2$. In addition, we consider the limit $\delta_m \to 0$ and replace the forces due to motor stretching by the force μ

29

which represents the Lagrange multiplier for the constraint

$$z(m_1, t) = z(m_2, t). \tag{A.5}$$

This yields the ordinary differential equations

$$\frac{\mathrm{d}m_1}{\mathrm{d}t} = V_m \left[1 - \frac{\mu}{F_s} \frac{z_1 - z_2}{\|z_1 - z_2\|} \cdot z_1'(m_1, t) \right], \tag{A.6a}$$

$$\frac{\mathrm{d}m_2}{\mathrm{d}t} = V_m \left[1 + \frac{\mu}{F_s} \frac{z_1 - z_2}{\|z_1 - z_2\|} \cdot z_2'(m_2, t) \right], \tag{A.6b}$$

which are force-balance equations for the myosin motor positions $m_1(t)$ and $m_2(t)$. The equations (A.6) represent that unloaded motors (for which $\mu = 0$) move at the free-moving velocity, V_m. As the motor moves, it is exposed to stretching forces, with magnitude given by the Lagrange multiplier μ. The term involving the dot product is the projection of this force onto the direction of motor movement along the i-th filament. Assuming a linear force–velocity relationship its ratio with the stall force, F_s, determines the reduction of motor speed due to stretching forces.

For the filament equations (A.4b) and (A.4d), in addition to $\delta_m \to 0$, we also let $\delta_a \to 0$ enforcing the constraints

$$|z_i'| = 1, \quad i = 1, 2. \tag{A.7}$$

We write the limits of $2(|z_i'| - 1)/\delta_a$ as λ_i and apply integration by parts to remove derivatives of δz_i from under the integral sign. This yields

$$\int \kappa_a z_i'' \cdot \delta z_i'' + \lambda_i z_i' \cdot \delta z_i' \, \mathrm{d}s = \int \delta z_i \cdot \left[\kappa_a z_i'''' - (\lambda_i z_i')' \right] \mathrm{d}s \\ + \delta z_i \cdot (\lambda_i z_i' - \kappa_a z_i''') + \kappa_a \delta z_1' \cdot z_i''. \tag{A.8}$$

We then rewrite equations (A.4b) and (A.4d) as

$$\int_0^{L_1} \delta z_1 \cdot \left[\frac{\lambda_a}{\Delta t} (z_1 - \boldsymbol{F} z_1^n) + \kappa_a z_1'''' - (\lambda_1 z_1')' + \mu \frac{z_1 - z_2}{\|z_1 - z_2\|} \delta (s - m_1) \right] \mathrm{d}s \\ + [\delta z_1 \cdot (\lambda_1 z_1' - \kappa_a z_1''') + \kappa_a \delta z_1' \cdot z_1'']_0^{L_1}, \tag{A.9a}$$

$$\int_0^{L_2} \delta z_2 \cdot \left[\frac{\lambda_a}{\Delta t} (z_2 - \boldsymbol{F} z_2^n) + \kappa_a z_2'''' - (\lambda_2 z_2')' - \mu \frac{z_1 - z_2}{\|z_1 - z_2\|} \delta (s - m_2) \right] \mathrm{d}s \\ + [\delta z_2 \cdot (\lambda_2 z_2' - \kappa_a z_2''') + \kappa_a \delta z_2' \cdot z_2'']_0^{L_2}, \tag{A.9b}$$

where δ is the Dirac delta function. The equations (A.9) enable us to derive the continuum governing equations and boundary conditions. First, we require the filaments to have zero curvature at their tips,

$$z_i'' = 0 \quad \text{at} \quad s = 0, L_i. \tag{A.10}$$

30

The remaining boundary terms in (A.9) then give rise to the conditions

$$\lambda_i z_i' - \kappa_a z_i''' = 0 \quad \text{at} \quad s = 0, L_i, \tag{A.11}$$

which specifies that the boundary values vanish at $s = 0, L_i$. Next, we apply the fundamental lemma of the calculus of variations to the remaining integrals. In the continuum limit $\Delta t \to 0$ for which $\boldsymbol{F} = \boldsymbol{I}$, and $(z_i - z_i^n)/\Delta t = \dot{z}_i$, we obtain

$$\lambda_a \frac{\partial z_1}{\partial t} + \kappa_a z_1'''' - (\lambda_1 z_1')' + \mu \frac{z_1 - z_2}{\|z_1 - z_2\|} \delta(s - m_1) = 0 \quad \text{on} \quad (0 < s < L_1), \tag{A.12a}$$

$$\lambda_a \frac{\partial z_2}{\partial t} + \kappa_a z_2'''' - (\lambda_2 z_2')' - \mu \frac{z_1 - z_2}{\|z_1 - z_2\|} \delta(s - m_2) = 0 \quad \text{on} \quad (0 < s < L_2). \tag{A.12b}$$

The differential equations (A.6) and (A.12), and conditions (A.10) and (A.11) as well as the constraints (A.5) and (A.7) then define a system of force-balance equations and boundary conditions that govern the evolution of two inextensible, semi-flexible filaments connected to an inextensible motor. This is the dimensional PDE model (2.14)–(2.16) given in the main text.

B Asymptotic Analysis

In this Appendix, we present the asymptotic analysis of §3 in more detail. We first outline the method used to solve the leading-order problem (3.6), and subsequently consider the $\mathcal{O}(\varepsilon)$ problem (3.14) for the first-order corrections.

B.1 Leading-Order Problem

We commence the analysis by considering the ansatz for rigid filaments. Taking the time derivative of (3.3) gives $\partial_t z_0' = -z_0'^\perp \dot{\theta}/2$, and taking four spatial derivatives of (3.7) yields $z_1^{(5)} = h^{(5)} z_0'^\perp$. Next, we can differentiate the governing equation of $\mathcal{O}(1)$ (3.6a) once with respect to s, and substitute the two above expressions to obtain

$$-z_0'^\perp \frac{\dot{\theta}}{2} + h^{(5)} z_0'^\perp - \lambda_0'' z_0' + \mu_0 \begin{pmatrix} 1 \\ 0 \end{pmatrix} \delta'(s - m_0) = 0. \tag{B.1}$$

We can now multiply the boundary condition (3.6c) by z_0', and use the property $z_1''' \cdot z_0' = 0$, which follows from (3.6e), to obtain $\lambda_0(0) = \lambda_0(1) = 0$. Finally, multiplying (B.1) by z_0' implies that

$$\lambda_0 = \mu_0 \begin{pmatrix} 1 \\ 0 \end{pmatrix} \cdot z_0' \left(H(s - m_0) - s \right) = H(s - m_0) - s, \tag{B.2}$$

31

where $H(s)$ denotes the Heaviside step function. The Lagrange multiplier $\mu_0 = 1/\sin(\theta/2)$, by rearranging (3.6b). The leading-order bulk stress is then

$$\sigma_0 = -2\int_0^1 \lambda_0 \, \mathrm{d}s = -2\mu_0 \sin\left(\frac{\theta}{2}\right)\left(\frac{1}{2} - m_0\right) = -2\left(\frac{1}{2} - m_0\right) = 2\nu_0, \qquad \text{(B.3)}$$

448 where $\nu_0 = m_0 - 1/2$. This completes the derivation of the quantities listed in (3.8).

We now derive the ordinary differential equations (3.9) for y_0, θ, and ν_0, the three degrees of freedom that govern the leading-order filament position, z_0. On taking the time derivative and variation, the ansatz (3.5) implies that

$$\partial_t z_0 = \begin{pmatrix} 0 \\ \dot{y}_0 \end{pmatrix} - z_0' \dot{m}_0 - z_0'^{\perp}(s - m_0)\frac{\dot{\theta}}{2}, \qquad \text{(B.4a)}$$

$$\delta z_0 = \begin{pmatrix} 0 \\ \delta y_0 \end{pmatrix} - z_0' \delta m_0 - z_0'^{\perp}(s - m_0)\frac{\delta\theta}{2}. \qquad \text{(B.4b)}$$

Integrating (3.6a) against δz_0 then yields

$$0 = \int_0^1 \partial_t z_0 \cdot \delta z_0 \, \mathrm{d}s + \mu_0 \begin{pmatrix} 1 \\ 0 \end{pmatrix} \cdot \left(\begin{pmatrix} 0 \\ \delta y_0 \end{pmatrix} - z_0' \delta m_0\right)$$

$$= \int_0^1 \partial_t z_0 \cdot \delta z_0 \, \mathrm{d}s - \mu_0 \sin(\theta/2)\delta m_0$$

$$= \int_0^1 \partial_t z_0 \cdot \delta z_0 \, \mathrm{d}s - \delta m_0. \qquad \text{(B.5)}$$

Substituting (B.4) into (B.5) then gives

$$0 = \int_0^1 \left(\begin{pmatrix} 0 \\ \dot{y}_0 \end{pmatrix} - z_0' \dot{m}_0 - z_0'^{\perp}(s - m_0)\frac{\dot{\theta}}{2}\right) \cdot \left(\begin{pmatrix} 0 \\ \delta y_0 \end{pmatrix} - z_0' \delta m_0 - z_0'^{\perp}(s - m_0)\frac{\delta\theta}{2}\right)\mathrm{d}s - \delta m_0$$

$$= \begin{pmatrix} 0 \\ \delta y_0 \end{pmatrix} \cdot \int_0^1 \left(\begin{pmatrix} 0 \\ \dot{y}_0 \end{pmatrix} - z_0' \dot{m}_0 - z_0'^{\perp}(s - m_0)\frac{\dot{\theta}}{2}\right)\mathrm{d}s - \delta m_0 \left(\begin{pmatrix} 0 \\ \dot{y}_0 \end{pmatrix} \cdot z_0' - \dot{m}_0\right)$$

$$- \int_0^1 \left(z_0'^{\perp} \cdot \begin{pmatrix} 0 \\ \dot{y}_0 \end{pmatrix} - (s - m_0)\frac{\dot{\theta}}{2}\right) \cdot (s - m_0)\frac{\delta\theta}{2}\mathrm{d}s - \delta m_0$$

$$= \delta y_0 \int_0^1 \left(\dot{y}_0 - \cos(\theta/2)\dot{m}_0 - \sin(\theta/2)(s - m_0)\frac{\dot{\theta}}{2}\right)\mathrm{d}s - \delta m_0\left(\dot{y}_0 \cos(\theta/2) - \dot{m}_0\right)$$

$$- \int_0^1 \left(\dot{y}_0 \sin(\theta/2) - (s - m_0)\frac{\dot{\theta}}{2}\right) \cdot (s - m_0)\frac{\delta\theta}{2}\mathrm{d}s - \delta m_0$$

$$= \delta y_0 \left(\dot{y}_0 - \cos(\theta/2)\dot{m}_0 - \sin(\theta/2)(1/2 - m_0)\frac{\dot{\theta}}{2}\right) - \delta m_0\left(1 + \dot{y}_0 \cos(\theta/2) - \dot{m}_0\right)$$

$$- \left(\dot{y}_0 \sin(\theta/2)(1/2 - m_0) - (1/3 - m_0 + m_0^2)\frac{\dot{\theta}}{2}\right)\frac{\delta\theta}{2}.$$

Collecting the coefficients of δy_0, $\delta\theta$ and δm_0, we obtain the system of differential equations (writing $\nu_0 = m_0 - 1/2$)

$$\dot{y}_0 = \left(12\nu_0^2 + 1\right)\cot\left(\frac{\theta}{2}\right)\csc\left(\frac{\theta}{2}\right), \tag{B.6a}$$

$$\dot{\theta} = -24\nu_0\cot\left(\frac{\theta}{2}\right), \tag{B.6b}$$

$$\dot{\nu}_0 = \csc^2\left(\frac{\theta}{2}\right)\left(1 + 6\nu_0^2(\cos(\theta)+1)\right), \tag{B.6c}$$

where $\csc(\phi) = 1/\sin(\phi)$. The equations (B.6b) and (B.6c) for θ and ν_0 are also independent of y_0, suggesting that the solution is invariant to vertical translations. Furthermore, the trigonometric functions can be eliminated by writing $S = \sin^2(\theta/2)$, which yields

$$\frac{\mathrm{d}S}{\mathrm{d}t} = -24\nu_0\left(1 - S\right), \tag{B.7a}$$

$$S\frac{\mathrm{d}\nu_0}{\mathrm{d}t} = 1 + 12\nu_0^2(1 - S). \tag{B.7b}$$

449   This completes the derivation of equation (3.9).

450   ## B.2   Higher-Order Corrections

To obtain the higher-order corrections, we first use the leading-order equation (B.1) and the ansatz (3.7) to solve for h, the curvature of z_1. Multiplying (B.1) by $z_0'^\perp$ and using $z_1''' \cdot z_0' = 0$ (which follows from (3.6e)), we obtain $h'''(0) = h'''(1) = 0$, and subsequently

$$-\frac{\dot{\theta}}{2} + h''''' - \mu_0\cos\left(\frac{\vartheta}{2}\right)\delta'(s - m_0) = 0. \tag{B.8}$$

The boundary conditions $h'''(0) = 0 = h'''(1)$ imply that

$$h''' = \frac{\dot{\vartheta}}{2}\frac{s(s-1)}{2} + \mu_0\cos\left(\frac{\vartheta}{2}\right)(H(s - m_0) - s) \tag{B.9}$$

and furthermore (since $z_1''(0) = 0 = z_1''(1)$), substituting for $\dot{\theta}$ and μ_0,

$$h'' = -\cot\left(\frac{\theta}{2}\right)\left[(m_0 - s)H(s - m_0) + s^2(m_0(2s - 3) - s + 2)\right], \tag{B.10}$$

451   which is an expression for filament curvature, $h''(s,t)$.

We now obtain the perturbation solution for the bulk stress, σ_1, which requires knowledge of the quantities μ_1 and λ_1. First, we integrate (B.10) once with respect to s. This introduces another constant of integration, here denoted $A(t)$, which might be

33

time-dependent and cannot be determined from boundary data. Consequently, we write

$$h'(s,t) = \tilde{h}'(s,t) + A(t), \tag{B.11}$$

where

$$\tilde{h}'(s,t) = \frac{\dot{\theta}}{2}\frac{s^3}{12}\left(\frac{s}{2} - 1\right) + \mu_0 \cos\left(\frac{\theta}{2}\right)\left(\frac{1}{2}(m-s)^2 H(s-m) - \frac{s^3}{6}\right). \tag{B.12}$$

Collecting the coefficients of ε in the governing equations with asymptotic expansions, we obtain the $\mathcal{O}(\varepsilon)$ problem (3.14). On taking a derivative of (3.14a) and substituting $z_1' = h'(s,t)z_0'^\perp = (A(t) + \tilde{h}'(s,t))z_0'^\perp$, we obtain

$$(\dot{A} + \partial_t\tilde{h}')z_0'^\perp + z_2''''' - ((\lambda_0(A + f'(t,s)))''z_0'^\perp + \lambda_1''z_0')$$
$$+\mu_1\begin{pmatrix}1\\0\end{pmatrix}\delta'(s-m_0) - \mu_0\begin{pmatrix}1\\0\end{pmatrix}\delta''(s-m_0)m_1 = 0. \tag{B.13}$$

Expanding the inextensibility constraint (3.14f) implies that $z_0' \cdot z_2^{(5)} = -(|z_1'|^2)^{(4)}/2$. Multiplying (B.13) by z_0', we obtain

$$-\frac{1}{2}(|z_1'|^2)^{(4)} - \lambda_1'' + \begin{pmatrix}1\\0\end{pmatrix}\cdot z_0'\left[\mu_1\delta'(s-m_0) - \mu_0\delta''(s-m_0)m_1\right] = 0. \tag{B.14}$$

We can integrate (B.14) twice and apply the boundary conditions (3.14c) to determine the constants of integration. This yields

$$\frac{1}{2}(|z_1'|^2)'' + \lambda_1 = \begin{pmatrix}1\\0\end{pmatrix}\cdot z_0'\left[\mu_1\left(H(s-m_0) - \frac{s}{L}\right) - \mu_0\delta(s-m_0)m_1\right], \tag{B.15}$$

which we can rearrange to obtain λ_1. To eliminate μ_1 from (B.15), we use (3.14b) to infer an expression for μ_1. Substituting the ansatzes (3.5) and (3.7) for z_0 and z_1 respectively, we obtain

$$0 = -\begin{pmatrix}1\\0\end{pmatrix}\cdot\left(\mu_1 z_0' + \mu_0 h'(s,t)z_0'^\perp(m_0,t)\right)$$
$$= -\left(\sin\left(\frac{\theta}{2}\right)\mu_1 - \cos\left(\frac{\theta}{2}\right)\mu_0 h'(m_0,t)\right),$$

and therefore

$$\mu_1 = \mu_0 h'(m_0,t)\frac{\cos(\theta/2)}{\sin(\theta/2)} = \mu_0(A + \tilde{h}'(m_0,t))\cot\left(\frac{\theta}{2}\right). \tag{B.16}$$

Substituting (B.16) into (B.15), we obtain

$$
\lambda_1 = \begin{pmatrix} 1 \\ 0 \end{pmatrix} \cdot z_0' \left[\left(\mu_0(A + \tilde{h}'(m_0,t)) \cot \left(\frac{\theta}{2} \right) \right) (H(s - m_0) - s) - \mu_0 \delta(s - m_0) m_1 \right]
$$
$$
- \frac{1}{2} \left(|z_1'|^2 \right)''
$$
$$
= \left(A + \tilde{h}'(m_0,t) \right) \cot \left(\frac{\theta}{2} \right) (H(s - m_0) - s) - \delta(s - m_0) m_1 - (z_1' \cdot z_1'')'. \tag{B.17}
$$

Using the simplified expression (B.17) for λ_1, we can write the first-order perturbation of the bulk stress (3.12), given by

$$
\sigma_1 = -2 \int_0^1 \left(|z_1''|^2 + \lambda_1 \right) \, ds
$$
$$
= -2 \int_0^1 |h''|^2 \, ds - 2 \left(A + \tilde{h}'(m_0,t) \right) \cot \left(\frac{\theta}{2} \right) \left(\frac{1}{2} - m_0 \right) + 2m_1, \tag{B.18}
$$

where $\tilde{h}'(m_0,t)$ is

$$
\tilde{h}'(m_0,t) = \frac{\dot{\theta}}{2} \frac{m_0^3}{12} \left(\frac{m_0}{2} - 1 \right) + \cot \left(\frac{\theta}{2} \right) \left(-\frac{m_0^3}{6} \right)
$$
$$
= \frac{1}{2} \left(-12(2m_0 - 1) \cot \left(\frac{\theta}{2} \right) \right) \frac{m_0^3}{12} \left(\frac{m_0}{2} - 1 \right) + \cot \left(\frac{\theta}{2} \right) \left(-\frac{m_0^3}{6} \right)
$$
$$
= \cot \left(\frac{\theta}{2} \right) \left(-\frac{m_0^3}{12} \right) \left[(12m_0 - 6) \left(\frac{m_0}{2} - 1 \right) + 2 \right]
$$
$$
= -\frac{1}{12} m_0^3 \left(6m_0^2 - 15m_0 + 8 \right) \cot \left(\frac{\theta}{2} \right). \tag{B.19}
$$

To solve for the first-order correction to the filament positions, z_1, we require an initial condition, here denoted $z_{I,1}(s) = z_1(s,0)$. To determine the asymptotic expansion of the initial condition (2.28c), we return to the force-balance equations (2.1), and its equivalent time-discrete energy minimisation problem for the functional (2.2). In this expression, the drag component (2.3) dominates when Δt is small. Therefore, we determine the leading order term in the asymptotic expansion of the initial condition $z_I = z_{I,0} + \varepsilon z_{I,0} + \ldots$ as the best approximation of z_I in L^2 among the straight fibres (3.5), that is

$$
z_{I,0} = \begin{pmatrix} 0 \\ y_{I,0} \end{pmatrix} + \begin{pmatrix} \sin(\theta_I/2) \\ \cos(\theta_I/2) \end{pmatrix} (s - m_{I,0}), \tag{B.20}
$$

where

$$
(m_{I,0}, y_{I,0}, \theta_I) = \operatorname{argmin}_{\bar{m},\bar{y},\bar{\theta}} \int_0^1 (z_{I,0} - z_I)^2 \, ds. \tag{B.21}
$$

452 Since we focus on pairs of initially straight fibres in this study, we set $z_I = z_{I,0}$.

35

A similar approach is available to determine z_1^I. Using the ansatz (3.7), we have

$$z_{I,1} = \begin{pmatrix} 0 \\ y_{I,1}(t) \end{pmatrix} - z'_{I,0}(t)m_{I,1} + z'^{\perp}_{I,0}\left(A_I(s - m_{I,0}) + \int_{m_{I,0}}^{s} \tilde{h}'(t,s)\,\mathrm{d}s \right), \qquad \text{(B.22)}$$

where

$$(m_{I,1}, y_{I,1}, A_I) = \mathrm{argmin}_{\bar{m},\bar{y},\bar{\theta}} \int_0^1 (z_{I,0} + \varepsilon z_{I,1} - z_I)^2 \,\mathrm{d}s. \qquad \text{(B.23)}$$

In the case where $z_{I,0} = z_I$ the term $z_{I,1}$ is minimal in L^2. Then, the degrees of freedom $m_{I,1}$, $y_{I,1}$, and A_I can be computed using

$$0 = \int_0^1 z_{I,1} \cdot \delta z_{I,1} \,\mathrm{d}s, \quad \text{where} \quad \delta z_{I,1} = \begin{pmatrix} 0 \\ \delta y_1 \end{pmatrix} - z'_{I,0}\delta m_1 + z'^{\perp}_{I,0}(s - m_{I,0})\delta A. \qquad \text{(B.24)}$$

When we set $\delta y_1 = y_0$, $\delta m_1 = \int_0^1 (m_0 - s)\,\mathrm{d}s$, and $\delta A = 0$, we find that

$$0 = \int_0^1 z_{I,1} \cdot \left[\begin{pmatrix} 0 \\ y_{I,0} \end{pmatrix} + z'_{I,0}(s - m_{I,0}) \right] = \int_0^1 z_{I,1} \cdot z_{I,0} \,\mathrm{d}s. \qquad \text{(B.25)}$$

It therefore holds that $J_1(0) = 0$.

To complete the derivation, we use the ansatz (3.7) with degrees of freedom $A(t)$, $y_1(t)$, and $m_1(t)$. Its variation and time-derivative are given by

$$\delta z_1 = \begin{pmatrix} 0 \\ \delta y_1 \end{pmatrix} - z'_0\delta m_1 + z'^{\perp}_0(s - m_0)\delta A, \qquad \text{(B.26a)}$$

$$\partial_t z_1 = \begin{pmatrix} 0 \\ \dot{y}_1(t) \end{pmatrix} + z'_0\left[-\dot{m}_1 + \frac{\dot{\theta}}{2}\left(A(t)(s - m_0) + \int_{m_0}^{s} \tilde{h}'(s,t)\,\mathrm{d}s \right) \right]$$

$$+ z'^{\perp}_0\left(\frac{\dot{\theta}}{2}m_1 + \dot{A}(t)(s - m_0) - A\dot{m}_0 + \int_{m_0}^{s} \partial_t \tilde{h}'(s,t)\,\mathrm{d}s - \tilde{h}'(m_0,t)\dot{m}_0 \right), \qquad \text{(B.26b)}$$

where $\tilde{h}'(m_0,t)$ is given in (B.19). A system of differential equations for m_1, A and y_1 can then be found integrating (3.14a) against δz_1. Using computer algebra, we obtained the

36

system

$$
\begin{aligned}
\frac{\mathrm{d}y_1}{\mathrm{d}t} = {} & \frac{1}{960} \csc^4\left(\frac{\theta}{2}\right) \Bigg(960 A \sin\left(\frac{\theta}{2}\right) \left(6\nu_0^2 \cos(\theta) + 6\nu_0^2 + 1\right) \\
& + \cos\left(\frac{\theta}{2}\right) \left(-8928\nu_0^7 + 9600\nu_0^5 - 720\nu_0^4 + 490\nu_0^3 + 2940\nu_0^2 + 3\nu_0(960m_1 - 17) + 240\right) \\
& - 3\cos\left(\frac{3\theta}{2}\right) \left(864\nu_0^7 - 960\nu_0^5 - 240\nu_0^4 + 30\nu_0^3 + 980\nu_0^2 + 3\nu_0 + 960\nu_0 m_1 + 80\right) \Bigg),
\end{aligned}
$$

$$
\begin{aligned}
\frac{\mathrm{d}m_1}{\mathrm{d}t} = {} & -\frac{1}{960} \csc^4\left(\frac{\theta}{2}\right) \Bigg(-5760 A\nu_0^2 \sin(\theta) - 480 A \sin(\theta) \\
& + 10\left(576\nu_0^7 - 624\nu_0^5 - 20\nu_0^3 + 3\nu_0 + 48\right)\cos(\theta) + 4608\nu_0^7 - 5040\nu_0^5 - 200\nu_0^3 \\
& - 1440\nu_0^2 + 21\nu_0 + 3\nu_0 \cos(2\theta)\left(384\nu_0^6 - 400\nu_0^4 + 480\nu_0 + 480m_1 + 3\right) - 1440\nu_0 m_1 - 480 \Bigg),
\end{aligned}
$$

$$
\begin{aligned}
\frac{\mathrm{d}A}{\mathrm{d}t} = {} & -\frac{1}{160} \cot\left(\frac{\theta}{2}\right) \csc^2\left(\frac{\theta}{2}\right) \Bigg(4\left(96\nu_0^5 - 120\nu_0^3 + 60\nu_0^2 + 245\right)\nu_0 \cos(\theta) \\
& + 576\nu_0^6 - 880\nu_0^4 + 720\nu_0^3 - 300\nu_0^2 - 900\nu_0 - 15 \Bigg).
\end{aligned}
$$

454 These ODEs govern the solution for z_1, the first-order correction to the filament shape.

37